



1 **Solar radiation estimation in West Africa: impact of dust conditions during**
2 **2021 dry season**

3

4 Léo Clauzel¹, Sandrine Anquetin¹, Christophe Lavaysse¹, Gilles Bergametti², Christel
5 Bouet^{2,3}, Guillaume Siour⁴, Rémy Lapere¹, Béatrice Marticorena⁴, Jennie Thomas¹

6

7 ¹Université Grenoble Alpes, IRD, CNRS, Grenoble-INP, IGE, 38000 Grenoble, France

8 ²LISA, Université Paris Cité and Univ Paris Est Créteil, CNRS, F-75013 Paris, France

9 ³Institut d'Ecologie et des Sciences de l'Environnement de Paris, UMR IRD 242, Univ Paris
10 Est Créteil–Sorbonne Université–CNRS–INRAE–Université Paris Cité, F-93143 Bondy,
11 France

12 ⁴LISA, Univ Paris Est Créteil, Université Paris Cité, CNRS, LISA, F-94010 Créteil, France

13

14 *Correspondence to:* Léo Clauzel (leo.clauzel@univ-grenoble-alpes.fr)



15 **Abstract**

16 The anticipated increase in solar energy production in West Africa requires high-quality solar
17 radiation estimates, which is affected by meteorological conditions and in particular the
18 presence of desert dust aerosols. This study examines the impact of incorporating desert
19 dust into solar radiation and surface temperature estimations. The research focuses on a
20 case study of a dust event in March 2021, which is characteristic of the dry season in West
21 Africa. Significant desert aerosol emissions at the Bodélé depression are associated with a
22 Harmattan flow that transports the plume westwards. Simulations of this dust event were
23 conducted using the WRF meteorological model alone, as well as coupled with the
24 CHIMERE chemistry-transport model, using three different datasets for the dust aerosol
25 initial and boundary conditions (CAM5, GOCART, MERRA2). Results show that considering
26 desert dust reduces estimation errors in global horizontal irradiance (GHI) by about 75%.
27 The dust plume caused an average 18% reduction in surface solar radiation during the
28 event. Additionally, the simulations indicated a positive bias in aerosol optical depth (AOD)
29 and PM₁₀ surface concentrations. The choice of dataset for initial and boundary conditions
30 minimally influenced GHI, surface temperature, and AOD estimates, whereas PM₁₀
31 concentrations and aerosol size distribution were significantly affected. This study
32 underscores the importance of incorporating dust aerosols into solar forecasting for better
33 accuracy.

34

35 **Short summary**

36 Solar energy production in West Africa is set to rise, needing accurate solar radiation
37 estimates, which is affected by desert dust. This work analyses a March 2021 dust event
38 using a modelling strategy incorporating desert dust. Results show that considering desert
39 dust cut errors in solar radiation estimates by 75% and reduces surface solar radiation by
40 18%. This highlights the importance of incorporating dust aerosols into solar forecasting for
41 better accuracy.

42

43 **1. Introduction**

44 The West African region is facing significant development challenges due to global change.
45 One of these challenges is related to access to electricity, particularly through the use of
46 renewable energy. West African countries have committed to reduce their greenhouse gas
47 emissions as part of the Paris Agreement (2015). Furthermore, assessments of solar
48 resources in West Africa demonstrate the region's substantial potential, as shown by
49 Diabaté et al. (2004), Plain et al. (2019) and Yushchenko et al. (2018). The International
50 Energy Agency (IEA) projects that the installed capacity for photovoltaic (PV) power
51 generation will increase by almost 20 times from 2020 to 2030 under its Sustainable Africa
52 Scenario (Africa Energy Outlook, IEA, 2022). PV energy is expected to experience
53 significant growth due to its competitiveness and low-carbon nature. However, solar
54 production is highly dependent on weather conditions (Dajuma et al., 2016).

55 The growth of solar energy in West Africa calls for the development of tailored tools to
56 facilitate its integration into power grids and ensure optimal operational maintenance.
57 Accurate production forecasts are required by solar power plant operators, spanning various
58 timescales, ranging from a few hours to several days. This is essential for maximising
59 production, reducing penalties linked to predicted deliverable energy, and optimising plant
60 maintenance to minimise production losses. High-quality forecasts are also crucial for
61 electricity grid operators to maintain supply-demand equilibrium and ensure system stability.
62 Therefore, the variability of energy production significantly affects them. The key



63 meteorological variables that influence photovoltaic production are the Global Horizontal
64 Irradiance (GHI) and the air temperature. These factors, which directly impact electricity
65 production and cell efficiency, often reach high levels in this region as demonstrated by
66 Dajuma et al. (2016) and Ziane et al. (2021). Their findings indicate that solar radiation is the
67 primary factor influencing PV production, as the generated current by the photoelectric effect
68 is proportional to the irradiance. Furthermore, they demonstrate that, at the second order,
69 the air temperature affects the efficiency of solar cells, as both parameters are inversely
70 correlated.

71

72 Clauzel et al. (2024) identified desert dust aerosol as a significant source of GHI forecast
73 errors for the only two solar power plants in the Sahel region of Sococim (Senegal) and
74 Zagtouli (Burkina Faso), particularly during the dry season. Dust aerosols are a key element
75 in the West African climate and strongly influence solar farm production through their direct
76 effect (aerosol-radiation interaction (ARI), Briant et al., 2017) and indirect effects (aerosol-
77 cloud interaction (ACI), Tuccella et al., 2019) on radiation, and also through their deposition
78 on solar panels (fouling effect, Diop et al., 2020, Aidara et al., 2023). As mentioned by Kok et
79 al. (2021), the West African desert aerosol load is the highest in the world and occurs mainly
80 during the dry season. In fact, North Africa, including the Sahara, is the world's largest
81 contributor to desert dust emissions (Prospero et al., 2002), and 60% of this dust is
82 transported to the West African region (D'Almeida, 1986; Kok et al., 2021). Most dust
83 emissions are associated with synoptic-scale atmospheric dynamics such as the Harmattan
84 flow during the dry season (Klose et al., 2010). Engelstaedter and Washington (2007)
85 pointed out the importance of small-scale wind events associated with the large-scale flow,
86 especially in the Bodele depression, which is a hotspot for dust emissions (Engelstaedter et
87 al., 2006). Analysing satellite observations, Schepanski et al. (2009) show that 65% of the
88 activation of the dust source area occurred in the early morning, demonstrating the important
89 role of the breakdown of the nocturnal low-level jet. Washington and Todd (2005) confirmed
90 the importance of the Bodele low-level jets during the dry season in initiating dust emissions
91 that can be transported to the West African coast within a few days. Dust aerosol emissions
92 are also highly linked to Mesoscale Convective Systems (MCS, Marsham et al., 2008 ;
93 Bergametti et al., 2017) and to strong near-surface winds in the intertropical discontinuity
94 zone during the rainy season (Bou Karam et al., 2009).

95

96 Some studies intend to model dust events in West Africa such as Ochiegbu (2021) who
97 implemented a back-trajectories model to understand the dust event reaching Nigeria. This
98 work revealed that most of the aerosols coming to Nigeria between 2011 and 2014 were
99 originating from the Bodele Depression. Menut (2023) focused on dust forecasting during the
100 Cloud-Atmospheric Dynamics-Dust Interactions in West Africa (CADDIWA) campaign during
101 summer 2021 (Flamant et al., 2024) using the CHIMERE regional chemistry-transport model
102 (Menut et al., 2021). The model was coupled online with the Weather Research and
103 Forecasting (WRF) meteorological model (Briant et al., 2017; Tuccella et al., 2019) to
104 perform dust aerosol concentration forecasts. The results of this work provide confidence in
105 the model coupling in the region as the dust forecast quality does not decrease with time
106 over a few days. In addition, only a limited number of studies have been conducted on the
107 prediction of GHI in the West African region. Sawadogo et al. (2024) conducted an
108 evaluation of WRF-solar GHI forecast (Jimenez et al., 2016) in Ghana for the year 2021. In
109 their work, a version of the model coupled offline with Copernicus Atmosphere Monitoring
110 Service (CAMS) Aerosol Optical Depth (AOD) forecasts was considered to integrate



111 information on aerosol load. They showed that WRF-Solar outperforms in predicting GHI
112 under clear sky conditions while its performance under high aerosol levels remains poor, that
113 was mainly attributed to uncertainties in the input AOD during data assimilation within the
114 model. Close to the region of interest, for the northern Morocco area, El Alani et al. (2020)
115 compared the performance of global models (Global Forecast System, Integrated Forecast
116 System, McClear) and demonstrated their proficiency in capturing GHI hourly temporal
117 variability.

118

119 As far as our knowledge is concerned, no studies have been conducted to assess online
120 coupled simulations between a meteorological model and an aerosol life cycle model
121 representing the emissions, the transport and the deposition in West Africa to estimate solar
122 radiation. This is despite the significant presence of desert dust, characterised by high
123 concentrations in the region. Additionally, scarce attention has been given to the significance
124 of initial and boundary conditions for conducting the aerosol model on the performance of
125 analysis simulations, and to our knowledge, investigating these aspects would represent a
126 novel contribution to research in the West African region.

127

128 Within this general context, the objectives of this study are two folds i) to evaluate the ability
129 to reproduce a dust event using a meteorological and dust life cycle model coupling
130 configuration, and ii) to investigate whether the performance of the simulations can be
131 enhanced by modifying the aerosol initial and boundary conditions employed, and to
132 estimate the uncertainty associated with this dataset selection with regard to the errors made
133 by the model. Section 2 introduces the case study, the simulation configuration, the data and
134 models selected for this work. In Section 3, the results are presented, beginning with the
135 variables of interest for solar production (GHI and surface air temperature), followed by the
136 variables associated with the desert aerosols (AOD, concentration, size distribution,
137 emissions). Section 4 gives main conclusions and draws some perspectives for this study.

138

139 **2. Material and methods**

140

2.1. Case study

141

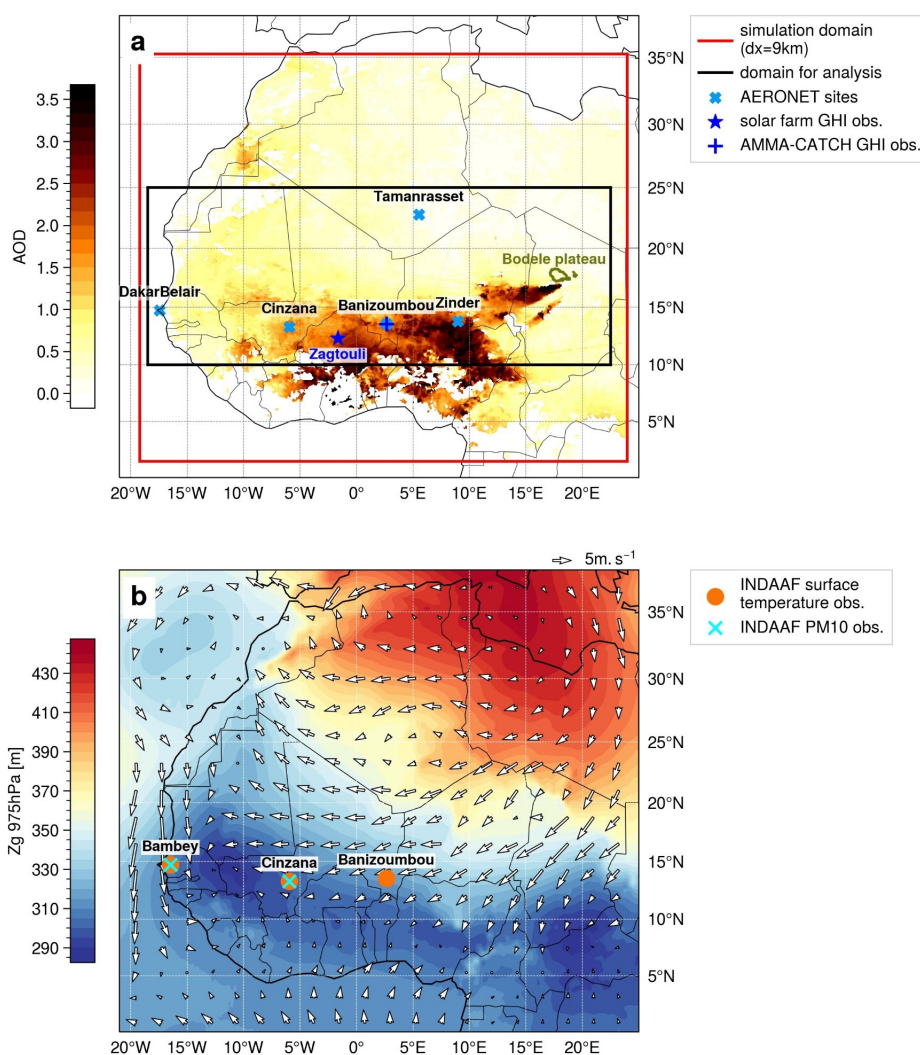
142 The case study is a dust event that occurs in West Africa from March 26th-00 UTC to April
143 2nd-00 UTC, 2021, i.e., during the dry season. High dust emissions occur at the Bodélé
144 Depression (Chad), the plume being then transported westward. The dust plume reached its
145 maximum intensity in terms of AOD and dust concentration over West Africa, and in
146 particular over the Zagtouli solar farm (Burkina-Faso, Fig. 1a), on March 30th. The event
147 was also chosen because it was not predicted in the solar forecast currently implemented for
148 the Zagtouli solar farm, leading to solar forecast errors during the passage of the dust plume
(Clauzel et al., 2024).

149

150 Figure 1 illustrates that this event is characterised by a strong Harmattan flow, with surface
151 winds from the South/South-West sweeping across the Bodélé Depression (Chad), where
152 the potential for desert dust emissions is very high (Prospero et al., 2002; Washington et al.,
153 2006). Additionally, this event is characterised by a westward flow between Chad and the
154 Atlantic coast, which facilitates the transportation of the dust plume. Fig. 1a shows
155 MODerate-resolution Imaging Spectroradiometer (MODIS) satellite observations of the AOD,
156 identifying the initial dust source area on the Bodélé Depression, as well as the westward
157 movement of the plume. This event is characteristic of the West African dry season
158 climatology, with a dominant Harmattan flow as described in the introduction. Figure S1
159 provides further insight into the dust plume transport during the case study.



159



160
 161 **Figure 1** - a) Mean aerosol Optical Depth at 550nm from MODIS satellite observations over
 162 the period 28 March-00 UTC to 02 April-00 UTC 2021. The Global Horizontal Irradiance
 163 (GHI) observations and AERONET aerosol measurement network, introduced in 2.4, are
 164 presented, as well as the boundaries of the simulated domain (red rectangle) and the area of
 165 interest for analysis (black rectangle). b) Mean synoptic conditions of the geopotential height
 166 (Zg) at 975hPa and the 10m-wind (white arrows - in m/s) over the period 28 March-00 UTC
 167 to 02 April-00 UTC 2021 from ERA5 reanalysis. The surface temperature and aerosol
 168 concentration observations from the INDAAF network, introduced in 2.4, are presented.

169

170

2.2. Modelling tools

2.2.1. WRF model

171



172 The meteorological Weather and Research and Forecasting model (WRF) model version
 173 3.7.1 is taken for compatibility with the CHIMERE coupling procedure. It is used in its non-
 174 hydrostatic configuration (Skamarock et al., 2008) and is forced at the boundaries of the
 175 domain every hour by the meteorological reanalysis data of ERA5 (ECMWF) provided on a
 176 regular 0.25° x 0.25° grid.

177 The model is run with a 9 km horizontal resolution, a 45s integration time step and 50
 178 vertical levels, from the surface to 50 hPa. The updated Rapid Radiative Transfer Model
 179 (RRTMG) radiation scheme (Iacono et al., 2008), which is mandatory for the aerosol optical
 180 properties feedback, is employed for both long- and short-wave radiations. Additionally, the
 181 Thompson aerosol-aware microphysics scheme (Thompson and Eidhammer, 2014) is
 182 applied. The Yonsei University planetary boundary layer's surface layer scheme (Hu et al.,
 183 2013) is also used, and the cumulus parameterisation is based on the Grell-Freitas scheme
 184 (Arakawa, 2004). The Revised MM5 surface layer scheme (Jiménez et al., 2012) is
 185 employed, while the Noah-MP Land Surface Model (Niu et al. 2011) is implemented for the
 186 land surface physics scheme.

187

188 2.2.2. CHIMERE model

189 The chemistry-transport model CHIMERE version v2020r3 (Menut et al., 2021) is used in
 190 conjunction with the WRF model. Both models have a 9 km horizontal grid. The CHIMERE
 191 model has 30 pressure-dependent vertical levels from the surface up to 200 hPa, with a first
 192 layer thickness of 3 hPa. The model is configured for dust-only, with no chemistry and only
 193 considering dust aerosols (details in section 2.3). The threshold friction velocities for dust
 194 emission are estimated using the Shao and Lu scheme (2000) and the 6-km spatial
 195 resolution GARLAP (Global Aeolian Roughness Lengths from ASCAT and PARASOL)
 196 dataset from Prigent et al. (2012). Mineral dust emission fluxes were calculated employing
 197 the Alfaro and Gomes (2001) scheme on 10 aerosol size bins ranging from 0.01 to 40 µm.
 198 The Fécan et al. (1999) parametrization is employed to account for the inhibitory effect of
 199 soil moisture on dust emission. Dry deposition is treated as described in Zhang et al. (2001).
 200 Wet scavenging for aerosol is computed following the Willis and Tattelman scheme (1989).
 201 The CHIMERE model includes the Fast-JX module, version 7.0b (Wild et al., 2000; Bian et
 202 al., 2002) for the calculation of radiative processes. It considers the radiative properties for
 203 each aerosol species and each aerosol size bin independently to compute the aerosol
 204 optical depths, the single scattering albedo and the aerosol asymmetry factor. More details
 205 on the dust aerosol radiative properties are given in Tables S1 and S2. Finally, we test three
 206 different initial and boundary condition datasets for mineral dust load (see 2.2.3).

207

208 **Table 1** - Parameterizations used in WRF and CHIMERE

WRF	
microphysics	Thompson aerosol-aware (Thompson and Eidhammer, 2014)
radiation	RRTMG scheme for LW and SW (Iacono et al., 2008)
land surface	Noah-MP land surface scheme (Niu et al., 2011)
planetary boundary layer	Yonsei University scheme



	(Hu et al., 2013)
surface layer	Revised MM5 surface layer scheme (Jimenez et al., 2012)
cumulus	Grell-Freitas scheme (Arakawa, 2004)
CHIMERE	
threshold friction velocities	Shao and Lu (2000) scheme
soil moisture	Fécan et al. (1999) scheme
dust emission fluxes	Alfaro and Gomes (2001) scheme
radiative processes	Fast-JX model, version 7.0b (Wild et al., 2000; Bian et al., 2002)
	0.010 - 0.022
	0.022 - 0.048
	0.048 - 0.107
	0.107 - 0.235
aerosol size distribution bins (diameters in μm)	0.235 - 0.516
	0.516 - 1.136
	1.136 - 2.500
	2.500 - 5.000
	5.000 - 10.00
	10.00 - 40.00

209

210

2.2.3. Dust aerosol initial and boundary condition datasets

211

In this study, the uncertainty in the solar estimate associated with the initial and boundary conditions of the dust aerosol load is evaluated. Three datasets were used: a climatology derived from the Global Ozone Chemistry Aerosol Radiation and Transport (GOCART, Ginoux et al., 2001), the Modern-Era Retrospective analysis for Research and Applications Version 2 (MERRA2) reanalysis (Gelaro et al., 2017) and the CAMS reanalysis (Inness et al., 2019).

217

The GOCART climatology is provided with the distribution of the CHIMERE model. It is a monthly climatology on a coarse horizontal grid ($2^\circ \times 2.5^\circ$), which is corrected by applying a factor of 0.3 as in Vautard et al. (2005).

220

The MERRA2 reanalysis combines the Goddard Earth Observing System (GEOS) and GOCART models, which are online coupled and implemented with a data assimilation system. It has a 3-hour temporal resolution and is presented on a $0.5^\circ \times 0.635^\circ$ horizontal grid. The observational data considered in the data assimilation process are AOD satellite observations from MODIS, Advanced Very High Resolution Spectroradiometer (AVHRR), Multi-angle Imaging SpectroRadiometer (MISR) and ground observations from the AEROSOL RObotic NETwork (AERONET).

227

The CAMS reanalysis was constructed using 4DVar data assimilation in ECMWF's Integrated Forecast System (IFS). It has a temporal resolution of 3 hours and is computed on a regular 0.75° horizontal grid. The AOD data from the Visible Infrared Imaging

229



230 Radiometer Suite (VIIRS), the MODIS and the Infrared Atmospheric Sounding Interferometer
231 (IASI) satellite observations are used as observational information in the data assimilation
232 process.

233 These three dust aerosol initial and boundary datasets differ in type (climatological or
234 reanalysis), in horizontal, vertical and temporal resolution, and in the resolution and range of
235 their aerosol size distribution. While GOCART has the highest number of aerosol classes
236 with 7 bins, CAMS covers a wider size spectrum despite a lower size resolution with only 3
237 classes. MERRA2 has an intermediate resolution with 5 classes, but covers a smaller
238 particle size spectrum than CAMS. The CHIMERE model pre-processes these dust aerosol
239 size distributions by applying a transfer coefficient δ to compute the dust aerosol
240 concentration on the 10 aerosol size bin defined for the simulations :

$$c_j = \sum_i \delta_{i,j} \times c_i \quad (1)$$

241 where c_i is the dust aerosol concentration of the i^{th} size bin from the initial and boundary
242 condition dataset considered, c_j is the dust aerosol concentration of the j^{th} size bin in the
243 CHIMERE simulation, and $\delta_{i,j}$ is the transfer coefficient. This transfer coefficient is derived
244 as :

- 245 - $\delta_{i,j} = 0$ if the i^{th} size bin from the initial and boundary condition dataset is found to be
246 wholly outside the j^{th} size bin in the CHIMERE simulation;
- 247 - $\delta_{i,j} = 1$ if the i^{th} size bin from the initial and boundary condition dataset is wholly
248 encompassed by the j^{th} size bin in the CHIMERE simulation;
- 249 - $\delta_{i,j} = \frac{\log(r_{j,max}) - \log(r_{j,min})}{\log(R_{i,max}) - \log(R_{i,min})}$ if the i^{th} size bin from the initial and boundary condition
250 dataset wholly encompasses the j^{th} size bin in the CHIMERE simulation;
- 251 - $\delta_{i,j} = \frac{\log(R_{i,max}) - \log(r_{j,min})}{\log(R_{i,max}) - \log(R_{i,min})}$ if the i^{th} size bin from the initial and boundary condition
252 dataset partially overlaps the j^{th} size bin in the CHIMERE simulation, but extends
253 below the start of this size bin;
- 254 - $\delta_{i,j} = \frac{\log(r_{j,max}) - \log(R_{i,min})}{\log(R_{i,max}) - \log(R_{i,min})}$ if the i^{th} size bin from the initial and boundary condition
255 dataset partially overlaps the j^{th} size bin in the CHIMERE simulation, but extends
256 beyond the end of this size bin;

257 where $R_{i,min}$ and $R_{i,max}$ are respectively the radius of the lower and upper limit of the i^{th} size
258 bin from the initial and boundary condition dataset, and $r_{j,min}$ and $r_{j,max}$ are respectively the
259 radius of the lower and upper limit of the j^{th} size bin in the CHIMERE simulation.

260

261 For the sake of simplicity, throughout this article, we will refer to the WRF-CHIMERE
262 simulations runned with the GOCART, the MERRA2, and the CAMS dust aerosol initial and
263 boundary conditions as *wrf_chimere-G*, *wrf_chimere-M*, and *wrf_chimere-C* simulations
264 respectively.

265 Table 2 summarises the characteristics of the three dust aerosol datasets and their
266 associated size distributions.

267



268 **Table 2.** Summary of the characteristics of the dust initial and boundary condition products.

	GOCART	MERRA2	CAMS
type	climatology	reanalysis	reanalysis
temporal resolution	monthly	3h	3h
vertical levels	20	72	60
horizontal resolution (lat x lon)	2°x2.5°	0.5°x0.635°	0.75°x0.75°
aerosol size distribution (radius in µm)	0.20 - 0.36 µm	0.1 - 1.0 µm	0.03 - 0.55 µm
	0.36 - 0.60 µm	1.0 - 1.8 µm	0.55 - 0.90 µm
	0.60 - 1.20 µm	1.8 - 3.0 µm	0.90 - 20.00 µm
	1.20 - 2.00 µm	3.0 - 6.0 µm	
	2.00 - 3.60 µm	6.0 - 10.0 µm	
	3.60 - 6.00 µm		
	6.00 - 12.00 µm		

269

270

2.3. Modelling strategy

271

272

273

274

275

276

277

278

279

280

281

282

283

284

285

286

287

288

289

290

291

292

293

The domain of simulation extends from 2° to 35°N and from 19°W to 24°E, as illustrated by the red box in Figure 1b. The domain is large enough to represent the primary atmospheric flows, including the Harmattan North/North-West flow and the monsoon South flow, as well as the transport of the emitted aerosol plumes. A horizontal resolution of 9 km has been selected in order to ensure that the grid ratio is approximately 3 with the ERA5 meteorological forcing. This choice is also motivated by the a priori intention to achieve a resolution higher than that of previous CHIMERE simulations performed in this region and compared to the operational solar forecast model used for the Zagtouli solar farm, which are based on global forecast models (see 2.4.1). The CHIMERE model is configured in a “dust only” model, which models only the mineral dust type. This hypothesis is supported for this dust case study by Fig. S2, as desert dust is the dominant aerosol during the event, particularly above 10°N. It is notable that biomass burning, which represents the other principal aerosol source in this region, is no longer a significant contributor to aerosol levels at that time of the year (Evans et al., 2018).

The WRF and CHIMERE models are coupled online through the OASIS3 MCT coupler. A two-way coupling strategy is selected, in which WRF sends meteorological variables to CHIMERE which in turn exchanges aerosol information such as AOD, Single Scattering Albedo (SSA) and Asymmetry Factor. This coupling strategy imposes most of the WRF parameterisations. The exchange frequency is set to 15 minutes. The WRF model computes fields on 50 levels, which are linearly interpolated over the 30 CHIMERE vertical levels via the OASIS coupler. The coupling includes the feedbacks of aerosol-radiation interactions (ARI, direct aerosol effect) and aerosol-cloud interactions (ACI, indirect aerosol effects) simultaneously.



294 The simulation starts on March 14th-00 UTC and ends on April 2nd-00 UTC, 2021. The first
295 two weeks served as the spin-up period. The simulation outputs are analysed for the period
296 of March 28th-00 UTC to April 2nd-00 UTC, which corresponds to the passage of the
297 dust plume in the Sahel region, in particular around the Zagtouli solar farm in Burkina Faso.
298 Four simulations were conducted: a meteorological simulation using WRF model alone, and
299 dust simulations with the coupled WRF-CHIMERE models using as initial and boundary
300 conditions the GOCART climatology, the MERRA2 reanalysis and the CAMS reanalysis. The
301 simulation using only WRF allows for the evaluation of the impact of taking into account dust
302 aerosols in estimating solar radiation. This is compared to the other three simulations, which
303 are also used to evaluate the uncertainties associated with the choice of the aerosol initial
304 and boundary condition dataset. A domain of interest, spanning 10°N to 25°N (Fig. 1a), was
305 selected for analysis and comparisons. This choice was guided by the dust plume trajectory
306 (Fig. S1) and the “dust only” hypothesis (Fig. S2).

307

308 **2.4. Evaluation datasets**

309 This section presents the local and regional data that are employed in the evaluation of the
310 simulations.

311

311 **2.4.1. GHI**

312 The Global Horizontal Irradiance (GHI) is the total shortwave irradiance from the Sun on a
313 horizontal surface on Earth. It is the sum of direct irradiance, which takes into account the
314 solar zenith angle, and diffuse horizontal irradiance. It is measured in $W.m^{-2}$ for the
315 wavelength range 0.3 - 3.0 μm .

316

317 The national electricity company of Burkina-Faso, Sonabel, operates a solar farm in Zagtouli
318 (12.31°N;1.64°W; Fig. 1a), approximately 15 km west of the capital, Ouagadougou. It has an
319 installed capacity of 34 MWp and contributes up to 4% of Burkina Faso's annual electricity
320 production. Ground GHI measurements from pyranometers are available at a temporal
321 resolution of 15 minutes for the Zagtouli solar plant and undergo pre-processing to ensure
322 quality control. This involves removing outliers and days with missing data, visually checking
323 the consistency of the measured values and selecting data corresponding to production
324 hours (positive values for solar radiation at the top of the atmosphere). Operational GHI
325 forecasts for this solar farm are computed by the French company Steadysun. These
326 forecasts are based on a multi-model, multi-member and multi-mesh grid aggregation, which
327 is derived from the NCEP Global Ensemble Forecast System and the ECMWF Integrated
328 Forecast System (Clauzel et al., 2024).

329 In-situ measurements of GHI from pyranometers (Fig. 1a) are also available at a 15-minutes
330 temporal resolution for the Banizoumbou (Niger) surface station, installed as part of the
331 AMMA-CATCH observatory (Analyse Multidisciplinaire de la Mousson Africaine - Couplage
332 de l'Atmosphère Tropicale et du Cycle Hydrologique, AMMA-CATCH (2005)).

333 The two measurement sites were selected because they are the only locations where GHI
334 observations have been made available along the dust plume transport for the case study,
335 with the Zagtouli power station being one of the first large solar farms in West Africa and the
336 AMMA-CATCH observatory being the only one to offer continuous GHI measurements for
337 the region and period of interest.

338

339 The CAMS gridded solar radiation dataset (CAMS solar radiation services v4.6, Schroedter-
340 Homscheidt et al., 2022), based on the Heliosat-4 method (Qu et al., 2017), provides several
341 variables related to solar radiation, such as clear-sky and all-sky GHI. It has a horizontal



342 resolution of $0.1^\circ \times 0.1^\circ$ and provides data every 15 minutes. The clear sky model includes
343 aerosols through the CAMS chemical transport model (Inness et al., 2019), which integrates
344 data assimilation of AOD and is coupled online to a numerical weather prediction model.
345 Cloud information for the all-sky model is derived from MeteoSat Second Generation (MSG)
346 satellite observations using the AVHRR Processing scheme Over cLOUDs, Land and Ocean
347 (APOLLO) Next Generation cloud processing scheme (Klüser et al., 2015). The dataset was
348 selected for comparison with the simulations as it integrates a description of aerosol
349 processes. While Yang and Bright (2020) show that it is the best performing product for
350 estimating surface solar radiation in the West African region among several satellite-based
351 gridded irradiance products, this dataset still has a negative bias of about 10% at desert
352 stations in North Africa (CAMS solar radiation regular validation report, 2020).

353

354

2.4.2. Surface temperature

355 In-situ surface temperature measurements are available for three stations of the
356 International Network to study Deposition and Atmospheric composition in Africa (INDAAF) :
357 Banizoumbou (Niger, 13.54° N, 2.66° E, 6.2m above surface; Rajot et al, 2010a; Marticorena
358 et al, 2010; Kaly et al., 2015), Cinzana (Mali, 13.28° N, 5.93° W, 2m above surface; Rajot et
359 al, 2010b; Marticorena et al, 2010; Kaly et al., 2015) and Bambey (Senegal, 14.70° N,
360 16.47° W, 5.2m above surface; Marticorena et al, 2021a) (Fig. 1b). The measurement sites
361 were selected since they are almost aligned around $13\text{-}15^\circ$ North, which represents the main
362 pathway of Saharan and Sahelian dust towards the Atlantic Ocean during the case study.
363 The ERA5 atmospheric reanalysis (Hersbach et al., 2020) provides spatially continuous
364 hourly values of surface temperature at 2 metres and has a horizontal resolution of $0.25^\circ \times$
365 0.25° .

366

367

2.4.3. Aerosol

368 The INDAAF network also provides data on aerosol concentration through ground
369 measurements of PM_{10} , i.e. the concentration of atmospheric particles having an
370 aerodynamic diameter less than $10 \mu\text{m}$. For this case study, hourly PM_{10} measurements are
371 available for two stations (Fig. 1b): Cinzana (Rajot et al, 2010c; Marticorena et al, 2021; Kaly
372 et al, 2015) and Bambey (Marticorena et al, 2021b).

373 The CAMS atmospheric reanalysis (Inness et al., 2019) is also used to evaluate regional
374 surface PM_{10} concentration and AOD. It provides 3-hourly data with a horizontal resolution of
375 $0.75^\circ \times 0.75^\circ$, with a surface layer thickness of 2.4 hPa.

376

377 Local ground measurements of AOD are retrieved from the AErosol RObotic NETwork level
378 1.5 dataset (AERONET, Holben et al., 1998; Giles et al., 2019). AOD is calculated from sun
379 photometer recordings, along with Ångström Exponent, and is only available during clear sky
380 conditions in daylight hours, with a resolution of 1 minute. The AOD at 400 nm simulated
381 with the WRF-CHIMERE model is converted to 440 nm for comparison with AERONET,
382 using the Ångström formula :

$$\frac{AOD_\lambda}{AOD_{\lambda_0}} = \left(\frac{\lambda}{\lambda_0} \right)^{-\alpha} \quad (2)$$

383 where AOD_λ is the AOD at the desired wavelength, $\lambda = 440 \text{ nm}$ here ; AOD_{λ_0} is the AOD at
384 the wavelength simulated in the model, $\lambda_0 = 400 \text{ nm}$ here ; α is the Ångström exponent,



385 derived from the simulated AOD at different wavelengths and here given for the range from
386 400 nm to 600 nm.

387 AERONET provides an aerosol size distribution dataset estimated through inversion of the
388 photometers data, as described in Dubovik and King (2000). The algorithm for inversion
389 provides a volume particle size distribution for 22 bins, which are logarithmically distributed
390 for radii between 0.05 μm and 15 μm .

391 The locations of the five AERONET sites used for comparison in this study are illustrated in
392 Figure 1a.

393

394 The spatially continuous AOD is also derived from level 2 aerosol products of MODIS Terra
395 and Aqua satellites (combined Dark Target, Deep Blue AOD at 0.55 micron, Collection 6.1,
396 Platnick et al., 2015). It provides a measure of the AOD at 550 nm during daytime for clear
397 sky conditions, with a spatial resolution of 10 km. To compare simulated AOD from WRF-
398 CHIMERE models with AOD from MODIS, the former is converted from 600 nm to 550 nm.
399 The conversion is performed using the Ångström formula (eq. 2).

400

401 Table 3 provides a general overview of the data used to evaluate the simulations in this
402 study.

403

404 **Table 3** - Summary of data used to evaluate the simulations.

	product	type	resolution
GHI	Zagtouli solar farm monitoring system	pyranometer GHI measurement	local
	AMMA-CATCH observational network	pyranometer GHI measurement	local
temperature	CAMS gridded solar radiation	atmospheric reanalysis	0.01°x0.01°
	INDAAF network	ground measurements	local
PM₁₀	ERA5	atmospheric reanalysis	0.25°x0.25°
	INDAAF network	ground measurements	local
Aerosol Size Distribution	CAMS (EAC4)	atmospheric reanalysis	0.75°x0.75°
	AERONET network	inversion product	local
Aerosol Optical Depth	AERONET network	sunphotometer ground measurements	local
	MODIS	satellite observations	10km

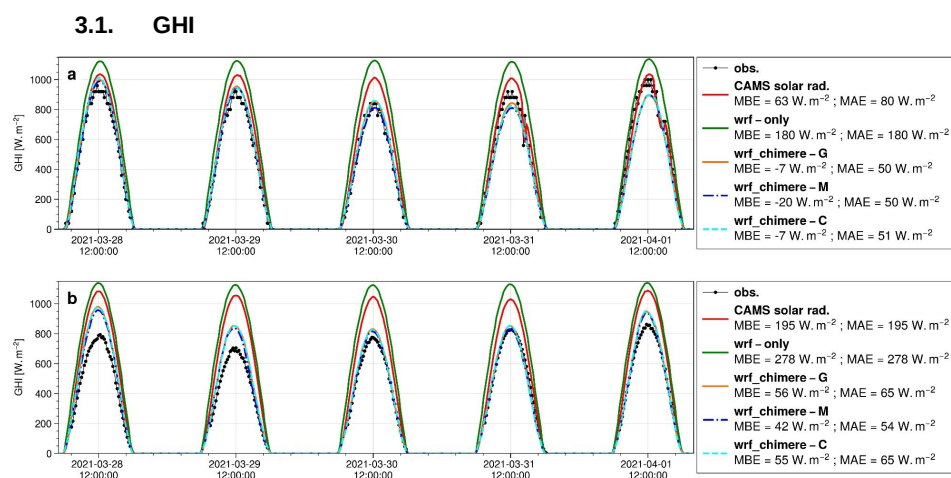
405

406 **3. Results**



407 The analysis starts by assessing the errors and uncertainties associated with the dust
 408 aerosol initial and boundary condition dataset employed to estimate the variables of interest
 409 for solar production, i.e. GHI and surface temperature. Subsequently, we investigate the
 410 potential causes of these uncertainties by evaluating the AOD, aerosol size distribution, and
 411 surface aerosol concentration (PM₁₀), as well as by examining mineral dust emissions and
 412 the flux of these aerosols at the boundaries of the domain. The metrics used to assess the
 413 quality of the simulations are described in Supplementary Materials.

414
 415



416

417 **Figure 2** - Local comparison of CAMS gridded solar radiation product and simulated GHI
 418 against a) the Zagtoui solar farm observations and b) the Banizoumbou AMMA-CATCH
 419 observations. *wrf_chimere-G*, *wrf_chimere-M* and *wrf_chimere-C* refer to the WRF-
 420 CHIMERE simulations using GOCART, MERRA2 and CAMS as dust aerosol initial and
 421 boundary condition dataset respectively.

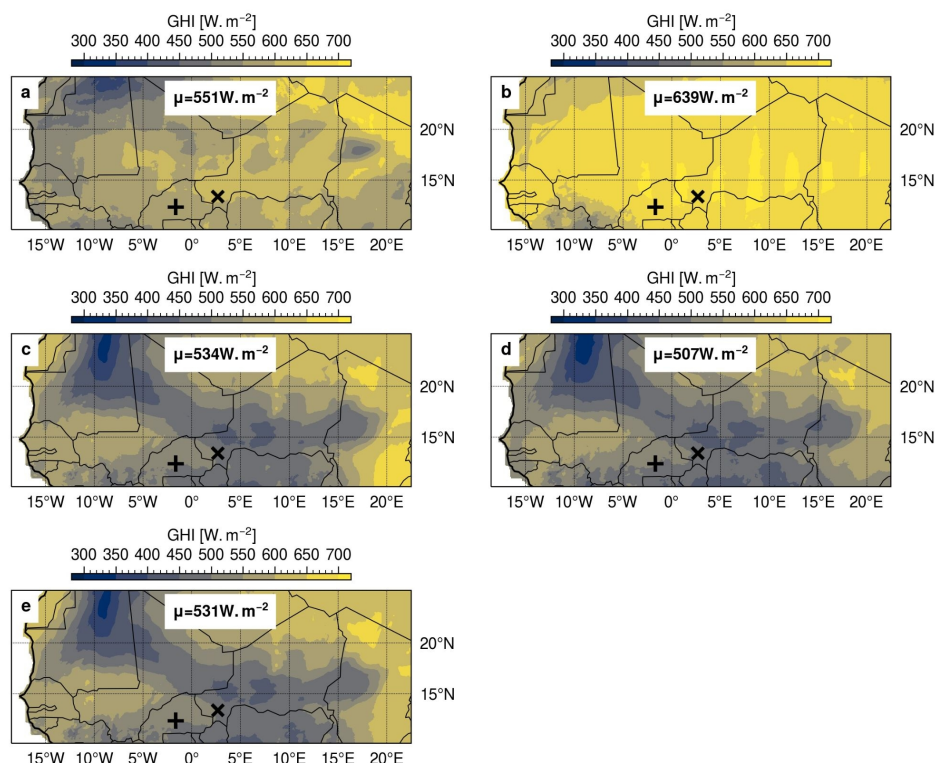
422

423 In Fig. 2, the local evaluation demonstrates the effect of taking into account dust aerosol for
 424 GHI estimation with the WRF-CHIMERE coupling over the WRF meteorological model
 425 alone. The coupling reduces the MAE by a factor of 3.6 at Zagtoui and by a factor of 4.6 at
 426 Banizoumbou on average. The simulations accurately represent the reduction in GHI
 427 intensity caused by the dust plume at both stations. However, the reduction persists
 428 compared to the observations at Zagtoui. At Banizoumbou, the simulations overestimate
 429 GHI at the beginning and end of the case study.

430 Figure 2 also indicates that the CAMS gridded solar radiation product fails to fully reproduce
 431 the dust event, with only a small reduction in GHI during the passage of the dust plume and
 432 an intermediate MAE between the WRF only and the WRF-CHIMERE simulations. This point
 433 serves to highlight the advantages of using a regional model in comparison to a global
 434 product for the simulation of dust conditions and the estimation of solar radiation.

435 Furthermore, the uncertainty in GHI estimation related to the choice of the dust aerosol initial
 436 and boundary condition dataset is limited, particularly when compared to the errors. This is
 437 evidenced by the fact that the mean standard deviation between the three WRF simulations
 438 is only 7% of the average MAE of these simulations at Zagtoui, and only 5% at
 439 Banizoumbou.

440



441

442 **Figure 3** - Mean day-time GHI during the period of 28 March-00 UTC to 02 April-00 UTC
 443 2021 as estimated by a) the CAMS gridded solar radiation dataset, b) the WRF only
 444 simulation, and the WRF-CHIMERE simulations with c) GOCART, d) MERRA2 and e)
 445 CAMS as dust aerosol initial and boundary condition dataset; + is the Zagtoui solar farm
 446 and x is the Banizoumbou site. μ is the mean GHI estimates over the domain.

447

448 The regional comparison presented in Fig. 3 provides more insight into the impact of
 449 incorporating dust on GHI estimation with the WRF-CHIMERE coupling, when compared to
 450 the WRF meteorological model alone. As anticipated the WRF-only simulation has the
 451 highest GHI estimates. The WRF-CHIMERE simulations indicate that dust aerosols reduce
 452 the mean GHI estimation by approximately $115 W.m^{-2}$ (-18%), while the CAMS gridded
 453 solar radiation global product shows a reduction of $88 W.m^{-2}$ (-14%). The three WRF-
 454 CHIMERE simulations exhibit identical regional patterns, with lower mean GHI values
 455 observed on the dust plume trajectory from the Bodélé Depression to the West, and also in
 456 the South Atlas region. In contrast, the CAMS gridded solar radiation dataset does not show
 457 this regional pattern, which may indicate that this global product does not fully capture the
 458 dust event.

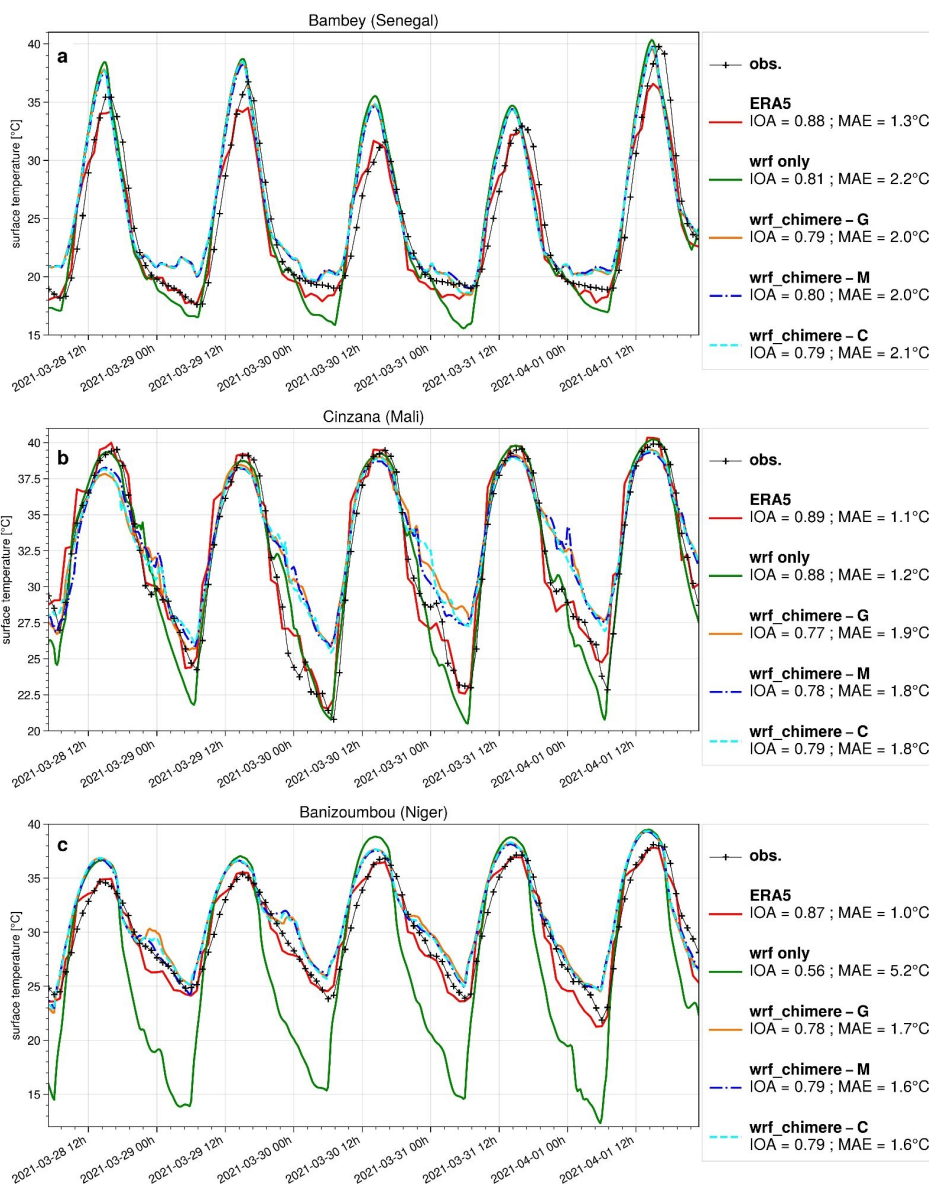
459 Furthermore, the uncertainty in GHI estimation associated with the choice of the dust aerosol
 460 initial and boundary conditions dataset is limited, particularly when compared to the changes
 461 brought by the taking of dust aerosol into account. Indeed, the standard deviation between
 462 the three WRF-CHIMERE simulations represents only 5% of the mean difference between
 463 these three simulations and the WRF-only simulation without dust.



464

465

3.2. Temperature



466

467 **Figure 4** - Local comparison of ERA5 and simulated surface temperature with the INDAAF

468 observations for a) Bambey (Senegal), b) Cinzana (Mali) and c) Banizoumbou (Niger)

469 measurement sites. *wrf_chimere-G*, *wrf_chimere-M* and *wrf_chimere-C* refer to the WRF-

470 CHIMERE simulations using GOCART, MERRA2 and CAMS as dust aerosol initial and

471 boundary condition dataset respectively. *IOA* is the Indicator of Agreement and *MAE* is the

472 Mean Absolute Error.

473



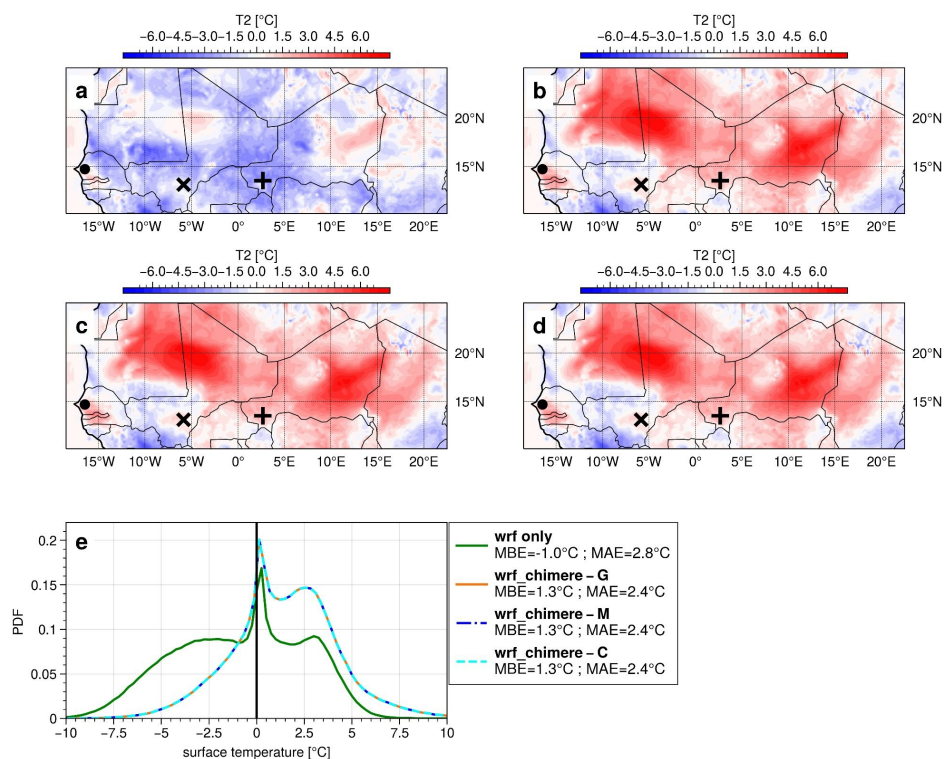
474 Figure 4 illustrates the contrasting outcomes of taking into account dust aerosols into the
475 WRF-CHIMERE coupling in comparison to the WRF meteorological model alone for the
476 estimation of surface temperature. At Bambey (Fig. 4a), which is far from the dust source
477 areas, the coupling has no effect on daytime temperatures but does affect night-time
478 temperatures. The WRF-CHIMERE and WRF-only simulations have IOA and MAE of the
479 same order of magnitude. At Cinzana (Fig. 4b), the WRF-only simulation performed better,
480 with a MAE 0.6°C lower than the coupled simulations, especially for night-time temperatures
481 but also for estimating the daily temperature peak. Finally, at Banizoumbou (Fig. 4c), which
482 is near the dust source areas, the coupling leads to a significant improvement in surface
483 temperature estimation, with an IOA of approximately 0.79 compared to 0.56 for the WRF-
484 only simulation and a MAE reduced by around 3.6°C. The impact of dust aerosols on
485 temperature is particularly pronounced at night-time. However, dust also affects the daily
486 temperature peak, with a reduction of 1.1°C of the daily maximum temperature observed on
487 the 30th of March.

488 Depending on the position of the measurement station, the results show a contrast, with a
489 significant improvement with the model coupling close to the source zones at Banizoumbou.
490 However, this improvement is reversed with increasing distance at Cinzana. This suggests
491 errors in the simulation of the transport of the dust plume from the source zones (Bodélé
492 Depression) towards the West. Overall, the main differences between WRF only and WRF-
493 CHIMERE coupled simulations occur at night time when there is no solar production. These
494 differences highlight the warming effect due to the dust aerosol interaction with the longwave
495 earth radiation.

496 In general, the uncertainty associated with the choice of the dust aerosol initial and boundary
497 condition dataset for the WRF-CHIMERE simulations is negligible compared to the errors in
498 temperature estimation or the difference with the WRF-only simulation.

499 The value of the ERA5 reanalysis for surface temperature evaluation is also reinforced in
500 Fig. 4, since it shows the lowest MAE and highest IOA. This dataset can therefore be
501 considered reliable for a regional evaluation of surface temperature.

502



503

504 **Figure 5** - Mean difference in surface temperature as compared to the ERA5 reanalysis for
 505 a) the WRF only simulation, the WRF-CHIMERE simulations with b) GOCART, c) MERRA2
 506 and d) CAMS as dust aerosol initial and boundary condition dataset, during the period of 28
 507 March-00 UTC to 02 April-00 UTC 2021; the black point is the Bambey, x is the Cinzana and
 508 + is the Banizoumbou INDAAF sites. e) Probability Density Function for the differences in
 509 surface temperature between simulations and the ERA5 reanalysis.

510

511 The regional surface temperature evaluation in Fig. 5 also reveals a contrast benefit of the
 512 coupling approach for the surface temperature estimation. While the WRF alone simulation
 513 (Fig. 5a) underestimates the surface temperature all over the domain, WRF-CHIMERE
 514 simulations are overestimating surface temperature in the dusty areas (Saharan region, Fig.
 515 5bcd). Overall, taking into account dust aerosol in the estimation of surface temperature
 516 reduces the MAE by 14% (Fig. 5e) when comparing the surface temperature estimates from
 517 simulations with the ERA5 reanalysis.

518

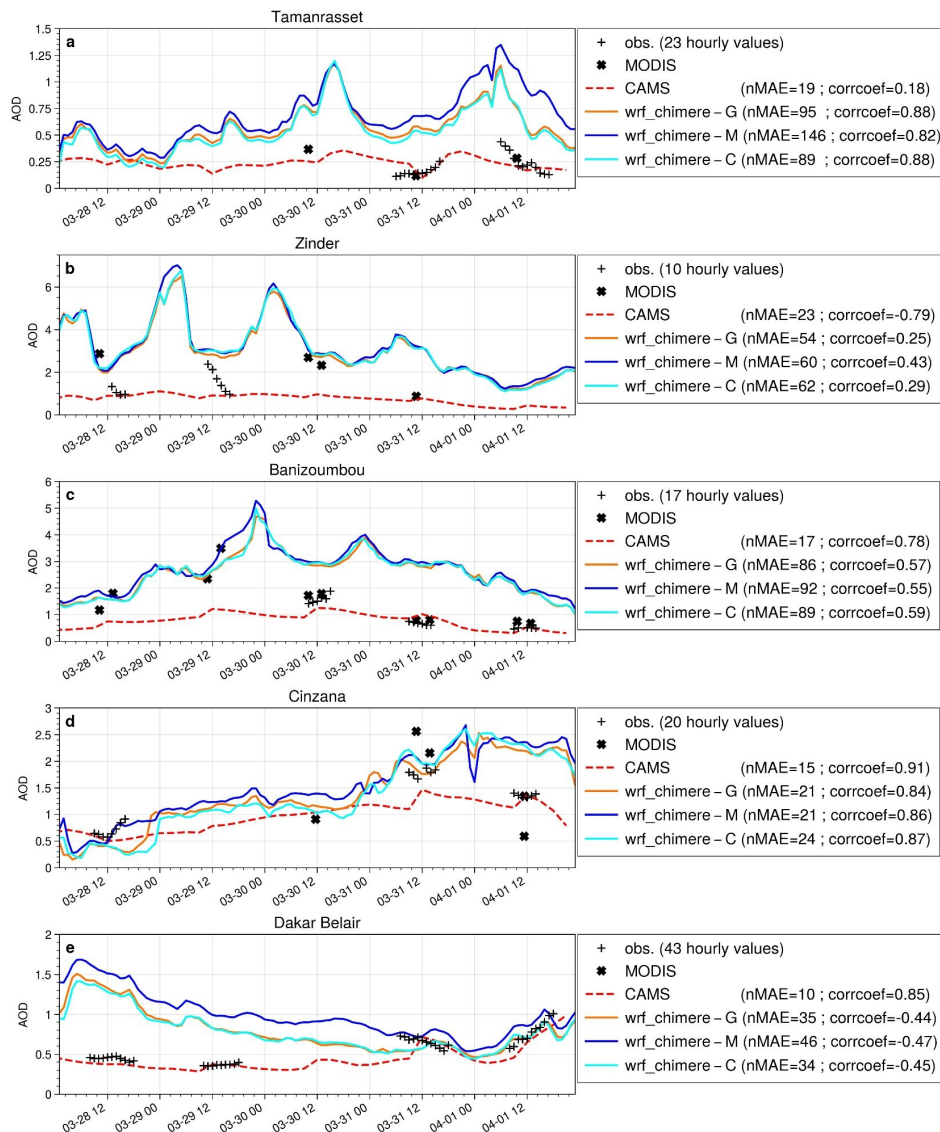
519 Furthermore, the uncertainty associated with the choice of the dust aerosol initial and
 520 boundary conditions dataset is limited. This is demonstrated by the fact that the standard
 521 deviation between the three WRF-CHIMERE simulations averaged over the period of
 522 analysis is 12% of the mean bias of those three simulations in comparison to ERA5
 523 reanalysis, and only 7% of the difference between the coupled simulations and the WRF-
 524 only simulation without dust.

524



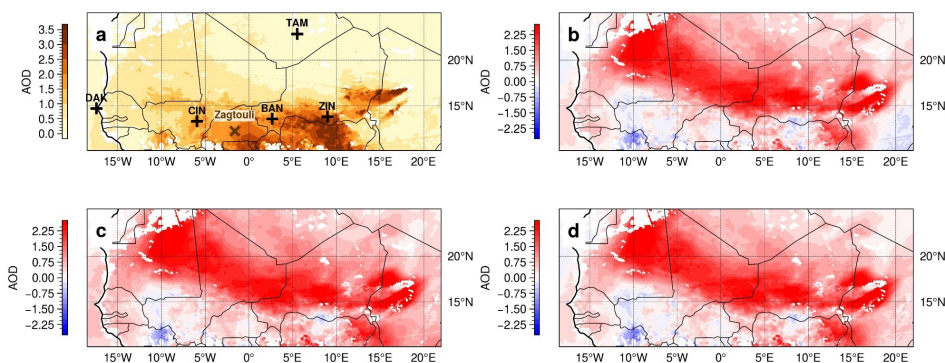
525 Finally, the incorporation of dust aerosol into the estimation of GHI appears to be a crucial
526 element in this case study. However, the value of this approach is more debatable in the
527 context of surface temperature estimation. Furthermore, the uncertainty related to the dust
528 aerosol initial and boundary condition dataset selection is limited, particularly when
529 compared to the simulation errors, and to the differences between including dust in the
530 simulation and not including it. The following sections will examine the simulated dust
531 aerosol condition during the case study in order to explain the discrepancies observed in
532 GHI and surface temperature, which are key parameters for solar production.
533
534

3.3. Aerosol Optical Depth





536 **Figure 6** - Local comparison of simulated AOD with AERONET in-situ measurements at 440
 537 nm for a) Tamanrasset, b) Zinder, c) Banizoumbou, d) Cinzana and e) Dakar Belair stations.
 538 *wrf_chimere-G*, *wrf_chimere-M* and *wrf_chimere-C* refer to the WRF-CHIMERE simulations
 539 using GOCART, MERRA2 and CAMS as dust aerosol initial and boundary condition dataset
 540 respectively; *MODIS* and *CAMS* refer to the AOD at 440 nm from the MODIS satellite
 541 observations and the CAMS atmospheric reanalysis respectively. *nMAE* is the normalised
 542 mean absolute error in % and *corrcoef* is the Person correlation coefficient, both derived
 543 with AERONET measurements as the reference.
 544 The local evaluations presented in Figure 6 reveal an overestimation of the AOD for stations
 545 close to dust sources such as Tamanrasset (Fig. 6a), Zinder (Fig. 6b) and Banizoumbou
 546 (Fig. 6c). This overestimation is more limited with increasing distance from the dust source
 547 at Cinzana (Fig. 6d) and Dakar (Fig. 6e). The order of magnitude of the dispersion between
 548 the three simulations is small when compared to the errors of the simulation in representing
 549 the observed AOD. As a consequence, the uncertainty associated with the choice of the dust
 550 aerosol initial and boundary condition dataset is limited. Overall, the AERONET AOD
 551 measurements appear to be very scarce, particularly close to the dust aerosol sources
 552 (Zinder, Tamanrasset, Banizoumbou, Cinzana). The AOD measurements are performed by
 553 sun photometers which give recording by pointing at the sun. Thus these recordings are only
 554 available during daytime and with clear sky conditions. In some cases of intense dust
 555 plumes with very high concentration, leading to strong solar radiation absorption, the sun
 556 photometers are technically limited and cannot produce any record or, sometimes, the
 557 AERONET quality control system removes them. This may be the reason for the scarcity of
 558 observations in this case study, which focuses on an intense dust event, increasing the
 559 perceived overestimation of the simulations. To compensate for this, the AOD estimates
 560 from MODIS satellite observations have been added to Figure 6 to complete the data.
 561 Furthermore, the CAMS reanalysis appears to be a reliable dataset for dust AOD estimation,
 562 as it has no overestimation and has the lowest *nMAE* for all sites. Although it does not
 563 reproduce the AOD dynamics close to the dust source at Tamanrasset and Zinder, it has the
 564 highest correlation coefficient for the other sites.
 565



566
 567 **Figure 7** - a) Mean from March 28th-00 UTC to April 2nd-00 UTC 2021 of MODIS AOD at
 568 550 nm satellite observations; x is the Zagtoui solar farm and + corresponds to AERONET
 569 stations. For panels b, c and d, AOD at 550 nm mean differences from March 28th-00 UTC
 570 to April 2nd-00 UTC 2021 between each of the WRF-CHIMERE simulations driven by
 571 GOCART, MERRA2 and CAMS, respectively, and the MODIS satellite observations.



572

573 The AOD differences shown in Fig. 7bcd show that the simulations significantly overestimate
574 the AOD as compared to the MODIS satellite observations, particularly in the Saharan and
575 North Sahelian zones and in the South Atlas, with an average overestimation of +1.25
576 between 15°N and 20°N. It is important to note that this overestimation is localised close to
577 the desert aerosol source zones. The simulated AOD error in the Sahel zone, particularly
578 around the Zagtouli solar power plant, is more limited with an average of +0.51 between
579 10°N and 15°N. The mean standard deviation between the three WRF-CHIMERE
580 simulations is only 10% of the mean error and 5% of the mean simulated AOD.
581 Consequently the uncertainty in the AOD estimate associated with the selection of the dust
582 aerosol initial and boundary condition dataset is small.

583 The observed overestimation of AOD by the WRF-CHIMERE simulations could be due to an
584 overestimation of the aerosol concentration, or to an inaccurate estimation of the size
585 distribution of the dust plume, or to excessive aerosol emissions within the domain, or to an
586 excessive inflow of desert aerosols at the domain boundaries. These hypotheses are
587 investigated below. Another potential explanation may also be the uncertainties in the
588 radiative properties of the dust aerosol incorporated in the CHIMERE model, or an
589 underestimation of the aerosol deposition flux; these aspects are not investigated here.

590

591 3.4. Aerosol size distribution

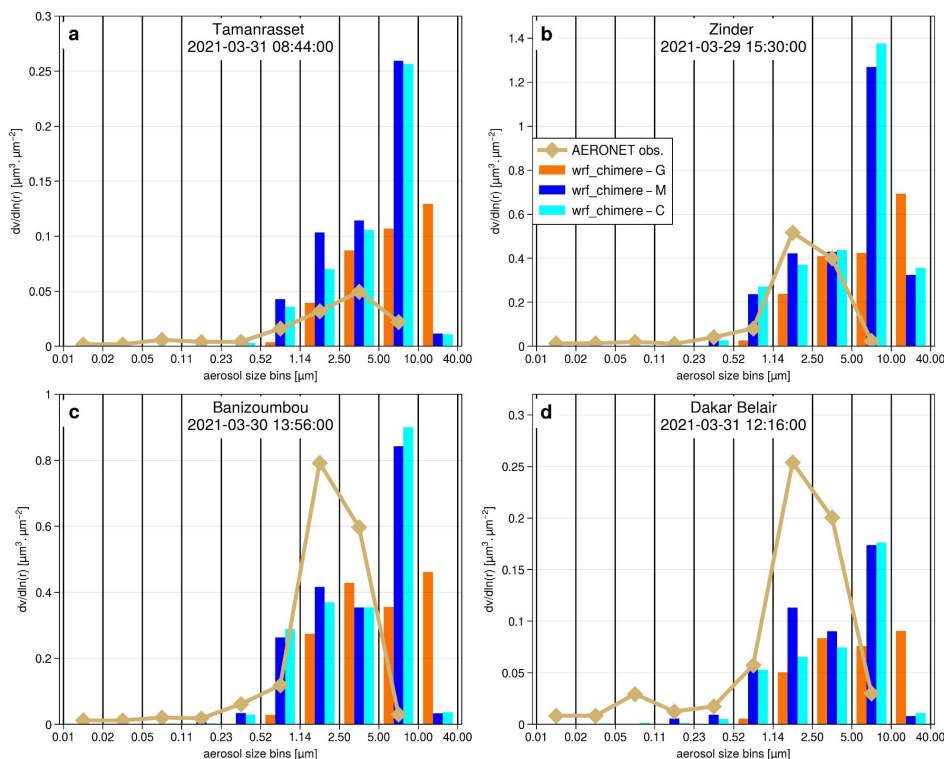
592 As presented in section 2, the AERONET inversion products provide aerosol size distribution
593 for 22 bins logarithmically distributed ranging from 0.05 to 15 µm. For comparison with the
594 modelled aerosol size distribution, this distribution is interpolated on the CHIMERE
595 simulations aerosol size distribution which is composed of 10 bins ranging from 0.01 µm to
596 40.00 µm in diameter (see Table 1). Given that the last bin (10.00-40.00 µm) is at the limit of
597 the capabilities of the inversion method, with a maximum wavelength at which the AOD is
598 measured of 875 nm, it is not shown for the AERONET dataset. Consequently, only
599 comparisons between the three simulations can be made for the bigger size section. The
600 column aerosol volume size distribution simulated by the model is calculated for each bin "i"
601 as in Menut et al. (2016) :

$$\frac{dV(r_i)}{d \ln(r_i)} = \sum_{k=1}^{n_{levels}} \frac{m_{k,r_i} \times \Delta z_k}{\rho_{dust} \times \ln(r_{i,max}/r_{i,min})} \quad (3)$$

602 where r_i is the mean mass median radius (in µm) and $r_{i,min}$ and $r_{i,max}$ the boundaries of the
603 i^{th} bin. m_{k,r_i} is the dust aerosol mass concentration (the mass of aerosol in one cubic metre
604 of air, in $\mu g \cdot m^{-3}$). ρ_{dust} is the dust aerosol density (the mass of the particle in its own volume,
605 $\rho_{dust} = 2300 \text{ kg} \cdot m^{-3}$). Δz_k is the model layer thickness (in metres), for a total of n levels (here
606 30 vertical levels).

607

608



609

610

Figure 8 - Aerosol volume size distribution for the AERONET station located in a) Tamanrasset, b) Zinder, c) Banizoumbou and d) DakarBelair. The time indicated corresponds to the time of the AERONET inversion product used for the comparison with the simulated aerosol size distribution. *wrf_chimere-G*, *wrf_chimere-M* and *wrf_chimere-C* refer to the WRF-CHIMERE simulations using GOCART, MERRA2 and CAMS as dust aerosol initial and boundary condition dataset respectively.

616

617

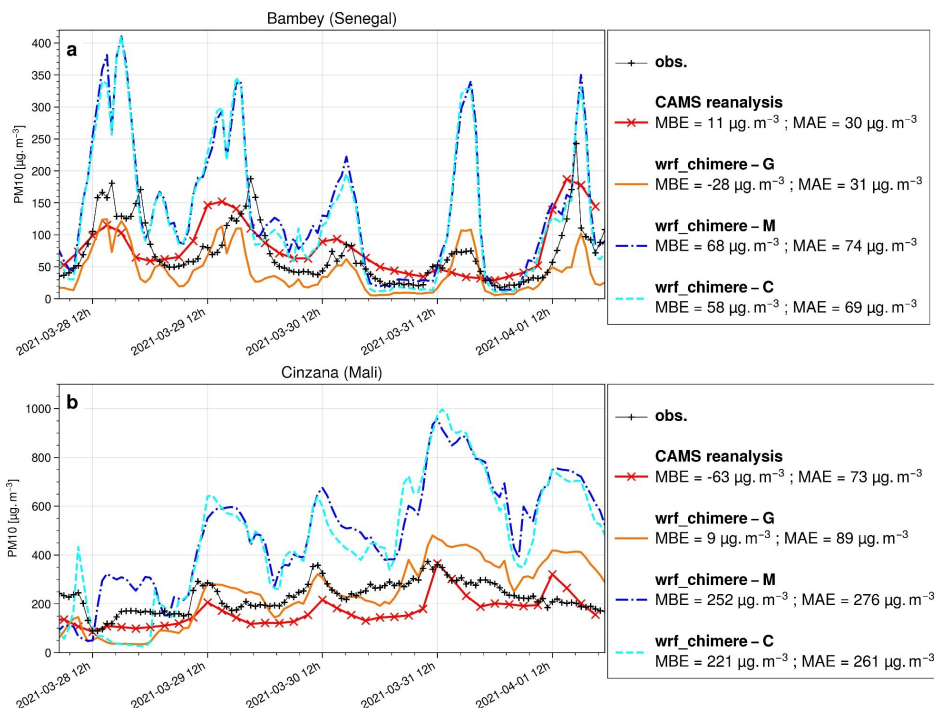
The evaluation of the aerosol size distribution in Fig. 8 shows that the simulations generally have a dominant aerosol size mode shifted towards coarser sizes compared to the AERONET inversion product. The ground-based size distribution has a strong peak between 1.14 μm and 5.00 μm , whereas the size distributions estimated by the WRF-CHIMERE simulations peak for coarser aerosol. For the Dakar Belair station (Fig. 8d), the AERONET inversion product indicates a first peak of lower intensity between 0.05 and 0.11 μm , which suggests the presence of aerosols other than desert dust. These aerosols may be of anthropogenic origin, given the proximity of the measurement site to the Senegalese capital. When comparing the size distributions between the three simulations with different dust aerosol initial and boundary condition dataset, it can be seen that the simulations driven with CAMS and MERRA2 reanalysis are relatively close and well separated from the one driven with the GOCART climatology. Notably, the dominant size bin in the simulation using GOCART dataset is consistently the largest particles, whereas with the aerosol from reanalyses, it is the aerosols between 5 μm and 10 μm . Consequently, the uncertainty associated with the selection of the dust aerosol initial and boundary condition dataset is high when examining the aerosol size distribution, particularly for particles exceeding 5.00



633 μm in diameter. The aforementioned uncertainties in the aerosol size distribution, which are
 634 linked to the choice of the dust aerosol initial and boundary conditions dataset, may be
 635 attributed to differences in the flow of desert dust entering the domain, as well as
 636 uncertainties in the transfer method carried out by the CHIMERE model to match the aerosol
 637 classes of these datasets to its own size distribution, described in section 2.2.3.
 638 As a result, the shift in the WRF-CHIMERE size distribution towards coarser particles
 639 compared to AERONET observations would result in a simulated AOD smaller than
 640 AERONET measurements. However, the opposite is observed (section 3.3). This suggests a
 641 positive bias in the simulated aerosol concentration, which would explain the positive bias in
 642 the AOD, while the coarser size distribution would tend to compensate.

643
 644

3.5. Aerosol concentrations



645

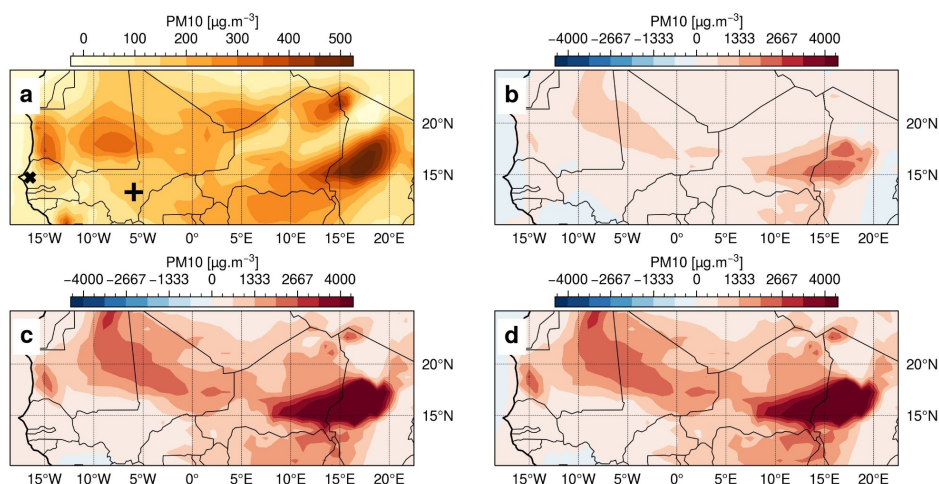
646 **Figure 9** - Local comparison of CAMS reanalysis and simulated PM_{10} surface concentrations
 647 with INDAAF network observations for a) Cinzana and b) Bambey stations. *wrf_chimere-G*,
 648 *wrf_chimere-M* and *wrf_chimere-C* refer to the WRF-CHIMERE simulations using GOCART,
 649 MERRA2 and CAMS as dust aerosol initial and boundary condition dataset respectively.
 650 MBE is the mean bias error and MAE refers to the mean absolute error.

651

652 The three simulations properly capture the dynamics of the PM_{10} surface concentration with
 653 respect to the INDAAF ground measurement (Fig. 9) as correlation coefficients are around
 654 0.6 at Cinzana and close to 0.7 at Bambey. The WRF-CHIMERE simulations driven with
 655 MERRA2 and CAMS dust aerosol datasets overestimate the surface PM_{10} concentration
 656 peaks for Bambey (Fig. 9a) and Cinzana (Fig. 9b), with high positive bias values of around
 657 63 $\text{g} \cdot \text{m}^{-3}$ at Bambey and 247 $\text{g} \cdot \text{m}^{-3}$ at Cinzana. The latter station is closer to the dust



658 aerosol sources. In contrast, the simulation using the GOCART dust aerosol dataset
 659 demonstrates superior performance in representing this variable, with an MAE that is
 660 approximately 60% and 70% lower than the two other simulations at Bambey and Cinzana,
 661 respectively.
 662 Furthermore, the uncertainty associated with the selection of initial and boundary condition
 663 dataset for dust aerosols is of a comparable magnitude to the simulation errors observed for
 664 surface PM₁₀ concentrations. Section 3.4 partly explains these discrepancies in surface PM₁₀
 665 concentration estimates between the simulation driven with the GOCART climatology and
 666 those driven with CAMS or MERRA2 reanalysis in terms of aerosol size distribution. These
 667 differences may also be attributed to variations in the size distribution of dust aerosol
 668 emissions or in the inflow of dust into the simulation domain and its aerosol size distribution.
 669 Furthermore, Fig. 9 indicates that the CAMS reanalysis provides reliable estimates of
 670 surface PM₁₀ concentration, as evidenced by the fact it has the lowest MAE values.
 671 However, the Bambey and Cinzana ground measurements, which are the only two available
 672 for the case study, are situated at a considerable distance from the dust sources, limiting our
 673 ability to assess the accuracy of the CAMS reanalysis in capturing the dust event. Moreover,
 674 the CAMS reanalysis exhibits a negative bias at Cinzana, which is the closest site to the dust
 675 sources.
 676



677
 678 **Figure 10** - a) Mean from March 28th-00 UTC to April 2nd-00 UTC 2021 of CAMS reanalysis
 679 PM₁₀ surface concentration; x refers to the Bambey and + corresponds to Cinzana INDAAF
 680 stations. For panels b, c and d, PM₁₀ surface concentration mean differences from March
 681 28th-00 UTC to April 2nd-00 UTC 2021 between each of the WRF-CHIMERE simulations
 682 driven by GOCART, MERRA2 and CAMS, respectively, and the CAMS reanalysis.
 683

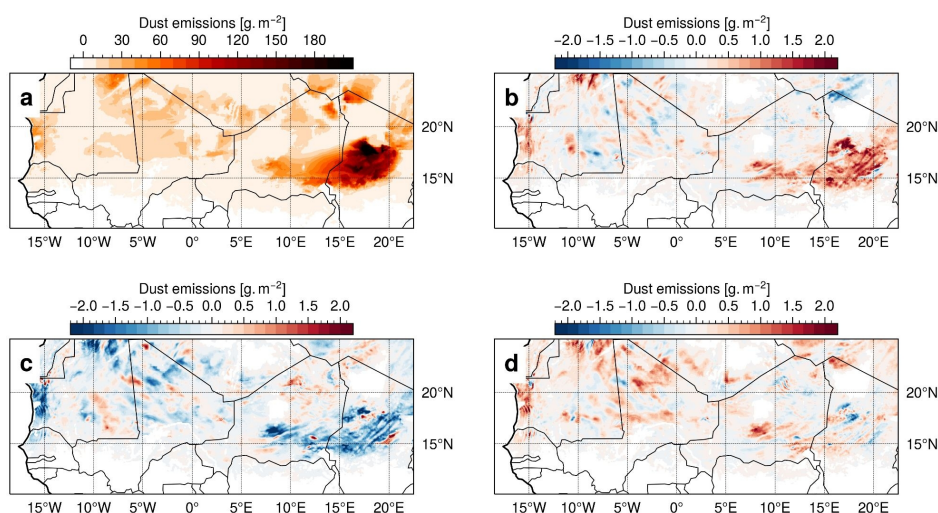
684 Figure 10 illustrates an overestimation of the PM₁₀ concentrations as compared to the CAMS
 685 reanalysis. This is particularly evident in dust source areas such as the Bodélé Depression.
 686 The WRF-CHIMERE simulation driven with the GOCART dataset is the closest to the CAMS
 687 reanalysis, with a mean estimate 3.6 times higher. However, this ratio reaches 8.6 for the
 688 simulations driven with the CAMS and MERRA2 reanalysis dataset.



689 The mean standard deviation between the three WRF-CHIMERE simulations is 35% of their
 690 mean PM_{10} surface concentration estimate. Consequently the uncertainty in the estimation of
 691 dust PM_{10} surface concentration associated with the selection of the dust aerosol initial and
 692 boundary condition dataset is significant. The discrepancies between the simulation using
 693 the GOCART climatology and the two other ones using CAMS or MERRA2 reanalysis can
 694 be partly explained by the differences in the simulated aerosol size distribution, as shown in
 695 section 3.4.

696
 697

3.6. Dust emissions



698

699 **Figure 11** - a) Total dust emissions flux from March 28th-00 UTC to April 2nd-00 UTC 2021,
 700 averaged between the three WRF-CHIMERE simulations. For panels b, c and d, total dust
 701 emissions individual differences between each of the WRF-CHIMERE simulations driven by
 702 GOCART, MERRA2 and CAMS, respectively, and the mean of the three WRF-CHIMERE
 703 simulations.

704

705 In terms of dust emissions (Fig. 11), the Bodélé Depression is, as expected, identified as
 706 the primary dust source area, with emissions reaching up to 244 g/m^2 . The differences of the
 707 simulations with each of the three dust aerosol initial and boundary conditions dataset,
 708 relative to their mean, exhibit highest values in the source zones located at the Bodélé
 709 Depression and the South Atlas. Nevertheless, it is worth noting that there is a factor of 100
 710 in between the emissions in the Bodélé area (approximately 200 g/m^2) and the observed
 711 differences between the three simulations. Consequently, the uncertainties in dust emissions
 712 resulting from the choice of the dust aerosol initial and boundary conditions dataset can be
 713 considered negligible. As emissions are primarily influenced by surface wind, it can be
 714 inferred that the uncertainty generated by the dust aerosol driving dataset on the surface
 715 wind is negligible too, which is confirmed by Fig. S4. Additionally, the size distributions of the
 716 aerosols emitted during the case study are found to be identical (not shown). Therefore, the
 717 differences in AOD and dust concentration may be attributed to the dust flows at the
 718 boundaries of the domain and are not linked to differences in simulated dust emissions
 719 within the domain. However, there is no observational data available to enable a quantitative



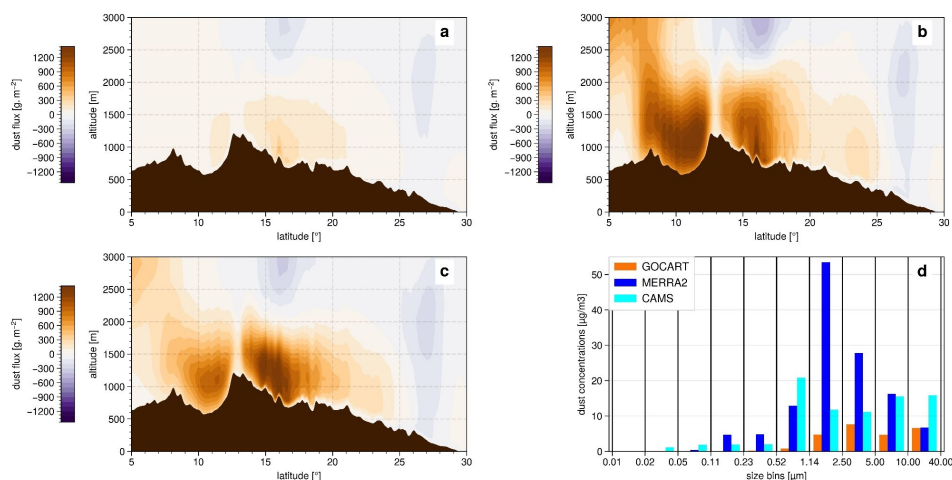
720 evaluation of the accuracy of the emissions computed within the WRF-CHIMERE
721 simulations.

722

723

3.7. Dust boundary flux

724



725

726 **Figure 12** - Cumul of the dust flux at the eastern boundary of the simulation from March
727 28th-00 UTC to April 2nd-00 UTC 2021 for the WRF-CHIMERE simulation with a) GOCART,
728 b) MERRA2 and c) CAM5 as dust aerosol initial and boundary conditions dataset; d) Dust
729 size distribution at the eastern boundary limit average during the case study period, from the
730 surface to 200hPa and over latitude. In panel abc, the dust flux is derived as the product
731 between the dust aerosol concentration and the zonal wind, and positive values of the dust
732 flow indicate a flow entering the simulation domain.

733

734 As shown in Fig. 1b, the dust event is associated with a strong Harmattan flow,
735 characterised by a northeasterly flow in the lower layer. It is thus interesting to quantify the
736 dust inflow associated with each of the dust aerosol initial and boundary conditions dataset
737 for the eastern domain boundary. The lowest dust flux is observed with GOCART (Fig. 12a),
738 with a maximum of approximately 480 g/m². In contrast, MERRA2 and CAM5 (Fig. 14 b
739 and c respectively) exhibit higher dust fluxes, with maximum values of around 1650 g/m².
740 The maximum flow is around 10°N for MERRA2, while for CAM5, it is closer to 16°N. Given
741 that GOCART is a climatology, it is reasonable to expect a lower dust flux compared to the
742 CAM5 and MERRA2 reanalyses, which are real case simulations incorporating data
743 assimilation of AOD. This is particularly true for the presented case study, which involves an
744 intense dust event associated with a Harmattan flow.

745 There are also significant differences in both quantity and distribution by aerosol size bin
746 (Fig. 12d). MERRA2 exhibits a strong dominant mode for the class between 1.14 µm and
747 2.50 µm, while CAM5 shows significant values from 0.52 µm to 40 µm, with a maximum for
748 the size class between 0.52 µm and 1.14 µm. Finally, the GOCART model displays a lower
749 variability between 1.14 µm and 40.00 µm, with the maximum occurring for the size class
750 between 2.55 µm and 5.00 µm.

751 The eastern dust fluxes at the boundary significantly vary depending on the dataset used as
752 dust aerosol initial and boundary conditions, both in terms of quantity and size distribution.



753 The reanalysis dataset, CAMS and MERRA2, are expected to provide a more accurate
754 representation of dust flux in terms of quantity as they are real case simulations assimilating
755 observational data in their calculations, as compared to GOCART which is a climatology.
756 However, GOCART provides a more comprehensive description of aerosol size distribution
757 with seven classes, in comparison to CAMS, which has only three classes but proposes a
758 higher horizontal resolution. While GOCART considers the effect of aerosol size to be
759 essential, CAMS assumes the horizontal resolution to be a key parameter. MERRA2 is the
760 most comprehensive of the three datasets, with the highest horizontal resolution, and an
761 aerosol size distribution that is close to the GOCART one with five classes. Despite the
762 absence of observational data that would permit a quantitative evaluation of the eastern dust
763 fluxes, the aforementioned elements suggest that the MERRA2 dataset might be more
764 accurate.

765 As a result, and in consideration of the negligible uncertainty in dust emissions within the
766 simulation domain related to the choice of the dataset for dust aerosol initial and boundary
767 conditions (see 3.6), these differences in eastern dust fluxes appear to account for the
768 uncertainties of the simulated aerosol concentrations (see 3.5) and AODs (see 3.3).

769

770 3.8. Discussions

771 The evaluation of the GHI at the Zagtouli solar power plant and the Banizoumbou site (Fig.
772 2) shows a clear improvement in its estimation when WRF is coupled to CHIMERE rather
773 than not as the local MAE is reduced by around 75%. This confirms the relevance of
774 incorporating the dust radiative effect with a coupling approach, in comparison with the
775 operational forecasts currently employed based on meteorological models alone. During the
776 dry season, dust events similar to the one presented here, with emissions at Bodélé and
777 then transport of the plume westwards, are common. This work therefore calls for
778 forecasters in the photovoltaic sector to better account for the desert dust cycle in their
779 forecast products. This local evaluation also highlights the potential benefits of using a
780 regional model rather than a global product, as the WRF-CHIMERE simulations outperform
781 the CAMS gridded solar radiation product with an average MAE reduced by approximately
782 38% at the Zagtouli solar farm and by 70% at the Banizoumbou site, which is closer to dust
783 sources. These discrepancies are corroborated by the regional comparison presented in
784 Figure 3, which reveals that the mean WRF-CHIMERE GHI estimate is 5% lower than the
785 CAMS solar radiation dataset. Additionally, the latter does not exhibit a geographical pattern
786 with lower GHI estimation along the dust plume trajectory, in contrast to the WRF-CHIMERE
787 simulations. Furthermore, the comparison indicates that the incorporation of dust in the
788 simulation reduces surface solar radiation by 18% for this case study. In light of the
789 anticipated expansion of PV production in West Africa, this point underscores the potential
790 consequences of such dust events if they are not accurately predicted.

791

792 The evaluation of local surface temperature (Fig. 4) reveals contrasting results regarding the
793 effectiveness of the coupled approach. It demonstrates an average local MAE reduction of
794 approximately 10% compared to the WRF-only simulation. However, the main differences
795 occur mainly at night, when no photovoltaic is produced. The regional evaluation in Fig. 5
796 confirms these contrasting results and indicates a reduction of regional MAE by about 14%
797 with the coupling rather than WRF alone. The overestimation of surface temperature in dusty
798 areas with the coupling, not present in the WRF only simulation, reveals the dominant
799 aerosol warming effect during night time as compared to the cooling effect during daytime.
800 These statements strongly depend on the accuracy of the ERA5 reanalysis which serves as



801 reference. ERA5 integrates data assimilation but does not consider aerosol information in its
802 calculation. Due to the limited ground measurements in the Saharan region to constrain the
803 reanalysis, it is possible that ERA5 underestimates the aerosol effect in dusty areas.

804

805 Nevertheless, despite the improvements demonstrated in solar radiation and surface
806 temperature estimation, the WRF-CHIMERE simulations exhibit a notable positive bias in
807 terms of AOD, as evidenced by the local and regional evaluations presented in Figs. 6 and
808 7. This overestimation cannot be attributed solely to differences in aerosol concentrations, as
809 the simulations yield markedly disparate surface concentrations of PM₁₀, depending on the
810 dust aerosol initial and boundary condition dataset chosen (Fig. 10) , while this
811 discrepancies do not appear in the AOD estimates. This excess of aerosol load may be
812 attributed to an overestimation of emissions within the domain, but this cannot be verified as
813 there is not any such measurement. The incoming flux of dust in the domain plays a minor
814 role as shown in Fig. 12 where the flux significantly also varies depending on the dust
815 aerosol initial and boundary condition dataset employed, while these differences are not any
816 more present in the simulated AOD estimates. Additionally, the underestimation of aerosol
817 deposition, by sedimentation (not studied in this research) could be at the origin of the
818 overestimation of the simulated dust loads. Finally, another potential explanation for these
819 AOD biases may be the inaccuracies in the dust radiative properties incorporated in the
820 CHIMERE model calculation (see Table S1 and S2). These depend on the mineralogical
821 composition of the desert dust particles emitted, which are considered uniform in this work.

822

823

824 The uncertainty associated with the choice of the large scale dust aerosol initial and
825 boundary condition dataset is very low when considering the variables of interest for solar
826 production, namely GHI and surface temperature (Fig. 3 and 5). This uncertainty is also low
827 compared to the performance of simulations for AOD estimation (Fig. 7). This result is similar
828 when examining dust emissions within the domain, which are nearly identical for the three
829 coupled simulations (Fig. 11). This can be explained by the fact that dust emissions depend
830 on the square of surface wind speed which present no significant signature of the selection
831 of the dust aerosol initial and boundary conditions (Fig. S4). The aerosols emitted within the
832 chosen domain are much greater than those entering, as the domain accounts for the main
833 source zones. This is why the simulations are not that sensitive to dust aerosol large-scale
834 dataset employed. The results regarding the uncertainty associated with the choice of the
835 dust aerosol initial and boundary condition dataset differs when examining various elements
836 of the dust life cycle. Indeed, aerosol size distributions vary significantly between the
837 simulation driven with GOCART on one hand, and simulations driven with CAMS and
838 MERRA2 on the other hand. GOCART climatology over-represents aerosols larger than 10
839 μm compared to the CAMS and MERRA2 reanalyses. These differences partially account
840 for the significant deviation in surface PM₁₀ concentration estimates (Fig. 10), indicating that
841 reanalysis-type datasets result in much higher values, up to 3 times higher, compared to
842 climatological-type data which is closer to ground observations. The dust flux entering the
843 domain may also partly explain these differences. In fact, this flux is very low with GOCART,
844 with values up to 3.5 times lower than CAMS and MERRA2 (Fig. 12). The size distribution of
845 this incoming aerosol flux is also a determining factor.

846

847 **4. Conclusion and perspectives**



848 This study aims to evaluate the ability of the WRF-CHIMERE coupling to simulate GHI
849 during a typical dust event in the dry season in West Africa. This event is characterised by a
850 Harmattan flux associated with significant desert dust emissions over the Bodélé
851 Depression, with the dust plume subsequently transported westward. This work
852 demonstrates the utility of coupling a meteorological model with a desert aerosol life cycle
853 model to represent such events, particularly for improving solar forecasts. Indeed, GHI
854 estimations are markedly enhanced with this approach compared to using a meteorological
855 model alone with a 75% reduction of local MAE. Nevertheless, the performance of the WRF-
856 CHIMERE simulations in representing the aerosol load of this event is more controversial.
857 There is an overall overestimation of AOD and PM₁₀ surface concentration by the coupled
858 model in the North Sahelian-Saharan zone.

859 This work also aims at investigating whether the performance of the simulations can be
860 improved by changing the dust aerosol initial and boundary condition dataset, and to
861 estimate the uncertainty associated with this choice. The results show that this selection has
862 almost no influence on the estimation of the solar radiation, surface temperature and AOD.
863 On the contrary, the choice of the dust aerosol initial and boundary condition dataset has a
864 significant impact on the surface PM₁₀ concentration and the aerosol size distribution.

865
866 This work outlines new research perspectives. Firstly, we observe the difficulty of evaluating
867 simulations in West Africa due to the scarcity of available observations. Establishing a
868 denser measurement network or conducting observation campaigns, particularly for GHI,
869 would help research on solar estimation and forecasting in this region. Additionally, the
870 WRF-CHIMERE simulations demonstrate significant biases in terms of AOD and PM₁₀
871 surface concentration which are not fully explained here. One potential explanation for this is
872 an overestimation of dust emission, for which no evaluation is possible. Furthermore,
873 studying aerosol deposition (not conducted in this work) would complement the study of the
874 desert aerosol life cycle. On the one hand, an underestimation of deposition might be a
875 contributing factor to the overestimation of the simulated aerosol load. On the other hand,
876 dust deposition on solar panels affects solar production by masking the available solar
877 radiation (soiling effect), and this should be taken into account in forecasting systems to
878 conduct optimised cleaning operations. Finally, the study focuses on a typical dust event
879 during the dry season, presenting essentially aerosol-radiation interaction. It could be
880 beneficial to test such simulation configuration for more complex cases involving cloud
881 presence. Indeed, the interaction between aerosols and clouds have a significant impact on
882 solar forecasting by increasing albedo, extending cloud lifespan, and promoting cloud
883 formation through increased condensation nucleus concentration (indirect aerosol effects).

884
885 **Code and data availability**

886 WRF namelist configuration files, CHIMERE parameter files, Python codes exploited in this
887 study and GOCART climatology data can be found on the following Zenodo repository:

888 <https://zenodo.org/records/10808476>

889 ERA5 data can be found on the Copernicus Climate Data Store service :

890 <https://cds.climate.copernicus.eu/cdsapp#!/home>

891 CAMS data were downloaded on the Copernicus Atmosphere Data Store service :

892 <https://ads.atmosphere.copernicus.eu/cdsapp#!/home>

893 MERRA2 data can be found on the dedicated platform from NASA :

894 <https://goldsmr5.gesdisc.eosdis.nasa.gov/data/MERRA2/>



895 Data from AMMA ground measurements stations can be accessed from the dedicated
896 website : <https://amma-catch.osug.fr/-jeux-de-donnees->
897 INDAAF web page allows access to the data : <https://indaaf.obs-mip.fr/catalogue/>
898 AERONET data measurements and inversion products are available through the following
899 link: <https://aeronet.gsfc.nasa.gov/>
900 The MODIS satellite observations are available on the “Level-1 and Atmosphere Archive &
901 Distribution System Distributed Active Archive Center” platform from NASA :
902 <https://ladsweb.modaps.eosdis.nasa.gov/>
903

904 **Author contributions**

905 LC, SA, CL conceptualised the study. LC performed the simulations, the analysis and the
906 editions of the figures. LC, SA, CL, GB, BM, GS, CB, RL and JT discussed the results. LC
907 wrote the paper
908

909 **Competing interest**

910 The contact author has declared that none of the authors has any competing interests.
911

912 **Acknowledgment**

913 This work has been supported by the NETWAT project (ANR-22-CE03-0011) operated by
914 the French National Research Agency. To conduct the simulations, this study has benefited
915 from access to the IPSL-SU (SPIRIT) cluster within the IPSL Mesocentre ESPRI facility,
916 supported by the CNRS, UPMC, Labex L-IPSL, CNES and Ecole Polytechnique. The
917 authors want to thank the WRF and CHIMERE developers for giving free access to their
918 model. We thank the National Aeronautics and Space Agency for the availability of the
919 MODIS and the MERRA2 data, the European Center for Medium-Range Weather Forecasts
920 for the availability of the CAMS and ERA5 data and the investigators and staff who maintain
921 and provide the AERONET, the INDAAF and the AMMA-CATCH observational data. Finally,
922 we thank the Sonabel company for their contribution.

923 During the preparation of this work the authors used DeepL Write (DeepL SE) in order to
924 improve language and readability. After using this tool/service, the authors reviewed and
925 edited the content as needed and take full responsibility for the content of the publication.
926

927 **References**

- 928 Africa Energy Outlook 2022, n.d.
- 929 Aidara, M.C., Fam, P.A., Danso, D.K., Mortey, E.M., Mbaye, A., Ndiaye, M.L.,
930 Bonkaney, A.L., Adamou, R., Anquetin, S., Diedhiou, A., 2023. Contribution to the
931 building of a weather information service for solar panel cleaning operations at
932 Diass plant (Senegal, Western Sahel). Open Geosciences 15.
933 <https://doi.org/10.1515/geo-2022-0449>
- 934 Alfaro, S.C., Gomes, L., 2001. Modeling mineral aerosol production by wind erosion:
935 Emission intensities and aerosol size distributions in source areas. Journal of
936 Geophysical Research: Atmospheres 106, 18075–18084.
937 <https://doi.org/10.1029/2000JD900339>
- 938 AMMA-CATCH (2005): Meteorological dataset (including radiative budget and soil
939 variables), within the Niamey square degree site (16 000 km²), Niger. IRD, CNRS-
940 INSU, OSUG, OMP, OREME. [doi:10.17178/AMMA-CATCH.AL.Met_Nc](https://doi.org/10.17178/AMMA-CATCH.AL.Met_Nc)



- 941 Arakawa, A., 2004. The Cumulus Parameterization Problem: Past, Present, and Future.
942 Journal of Climate 17, 2493–2525. [https://doi.org/10.1175/1520-](https://doi.org/10.1175/1520-0442(2004)017<2493:RATCPP>2.0.CO;2)
943 [0442\(2004\)017<2493:RATCPP>2.0.CO;2](https://doi.org/10.1175/1520-0442(2004)017<2493:RATCPP>2.0.CO;2)
- 944 Bergametti, G., Marticorena, B., Rajot, J.L., Chatenet, B., Féron, A., Gaimoz, C., Siour,
945 G., Coulibaly, M., Koné, I., Maman, A., Zakou, A., 2017. Dust Uplift Potential in the
946 Central Sahel: An Analysis Based on 10 years of Meteorological Measurements at
947 High Temporal Resolution. Journal of Geophysical Research: Atmospheres 122,
948 12,433–12,448. <https://doi.org/10.1002/2017JD027471>
- 949 Bian, H., Prather, M.J., n.d. Fast-J2: Accurate Simulation of Stratospheric Photolysis in
950 Global Chemical Models.
- 951 Bou Karam, D., Flamant, C., Tulet, P., Chaboureau, J.-P., Dabas, A., Todd, M.C., 2009.
952 Estimate of Sahelian dust emissions in the intertropical discontinuity region of the
953 West African Monsoon. Journal of Geophysical Research: Atmospheres 114.
954 <https://doi.org/10.1029/2008JD011444>
- 955 Briant, R., Tuccella, P., Deroubaix, A., Khvorostyanov, D., Menut, L., Mailler, S.,
956 Turquety, S., 2017. Aerosol–radiation interaction modelling using online coupling
957 between the WRF 3.7.1 meteorological model and the CHIMERE 2016 chemistry-
958 transport model, through the OASIS3-MCT coupler. Geoscientific Model
959 Development 10, 927–944. <https://doi.org/10.5194/gmd-10-927-2017>
- 960 Clauzel, L., Anquetin, S., Lavaysse, C., Tremoy, G., Raynaud, D., 2024. West African
961 operational daily solar forecast errors and their link with meteorological conditions.
962 Renewable Energy 224, 120101. <https://doi.org/10.1016/j.renene.2024.120101>
- 963 d’Almeida, G.A., 1986. A Model for Saharan Dust Transport. Journal of Applied
964 Meteorology and Climatology 25, 903–916. [https://doi.org/10.1175/1520-](https://doi.org/10.1175/1520-0450(1986)025<0903:AMFSDT>2.0.CO;2)
965 [0450\(1986\)025<0903:AMFSDT>2.0.CO;2](https://doi.org/10.1175/1520-0450(1986)025<0903:AMFSDT>2.0.CO;2)
- 966 Dajuma, A., Yahaya, S., Touré, S., Diedhiou, A., Adamou, R., Konaré, A., Sido, M.,
967 Golba, M., 2016. Sensitivity of Solar Photovoltaic Panel Efficiency to Weather and
968 Dust over West Africa: Comparative Experimental Study between Niamey (Niger)
969 and Abidjan (Côte d’Ivoire). Computational Water, Energy, and Environmental
970 Engineering 5, 123–147. <https://doi.org/10.4236/cweee.2016.54012>
- 971 Diabaté, L., Blanc, P., Wald, L., 2004. Solar radiation climate in Africa. Solar Energy 76,
972 733–744.
- 973 Diop, D., Drame, M.S., Diallo, M., Malec, D., Mary, D., Guillot, P., 2020. Modelling of
974 Photovoltaic Modules Optical Losses Due to Saharan Dust Deposition in Dakar,
975 Senegal, West Africa. Smart Grid and Renewable Energy 11, 89.
976 <https://doi.org/10.4236/sgre.2020.117007>
- 977 Dubovik, O., King, M.D., 2000. A flexible inversion algorithm for retrieval of aerosol
978 optical properties from Sun and sky radiance measurements. Journal of
979 Geophysical Research: Atmospheres 105, 20673–20696.
980 <https://doi.org/10.1029/2000JD900282>



- 981 Engelstaedter, S., Tegen, I., Washington, R., 2006. North African dust emissions and
982 transport. *Earth-Science Reviews* 79, 73–100.
983 <https://doi.org/10.1016/j.earscirev.2006.06.004>
- 984 Engelstaedter, S., Washington, R., 2007. Atmospheric controls on the annual cycle of
985 North African dust. *Journal of Geophysical Research: Atmospheres* 112.
986 <https://doi.org/10.1029/2006JD007195>
- 987 Evans, M., Knippertz, P., Akpo, A., Allan, R.P., Amekudzi, L., Brooks, B., Chiu, J.C.,
988 Coe, H., Fink, A.H., Flamant, C., Jegede, O.O., Leal-Liousse, C., Lohou, F.,
989 Kalthoff, N., Mari, C., Marsham, J.H., Yoboué, V., Zumsprekel, C.R., 2018. Policy
990 findings from the DACCIIWA Project. Zenodo.
991 <https://doi.org/10.5281/ZENODO.1476843>
- 992 El Alani, O., Ghennioui, A., Ghennioui, H., Saint-Drenan, Y.-M., Blanc, P., 2020.
993 Evaluation of 24-hours forecasts of global solar irradiation from IFS, GFS and
994 McClear models.
- 995 Fécan, F., Marticorena, B., Bergametti, G., 1998. Parametrization of the increase of the
996 aeolian erosion threshold wind friction velocity due to soil moisture for arid and
997 semi-arid areas. *Annales Geophysicae* 17, 149–157.
998 <https://doi.org/10.1007/s00585-999-0149-7>
- 999 Flamant, C., Chaboureaud, J.-P., Delanoë, J., Gaetani, M., Jamet, C., Lavaysse, C.,
1000 Bock, O., Borne, M., Cazenave, Q., Coutris, P., Cuesta, J., Menut, L., Aubry, C.,
1001 Benedetti, A., Bossler, P., Bounissou, S., Caudoux, C., Collomb, H., Donal, T.,
1002 Febvre, G., Fehr, T., Fink, A.H., Formenti, P., Araujo, N.G., Knippertz, P., Lecuyer,
1003 E., Andrade, M.N., Langué, C.G.N., Jonville, T., Schwarzenboeck, A., Takeishi, A.,
1004 2024. Cyclogenesis in the Tropical Atlantic: First Scientific Highlights from the
1005 Clouds–Atmospheric Dynamics–Dust Interactions in West Africa (CADDIIWA) Field
1006 Campaign. *Bulletin of the American Meteorological Society* 105, E387–E417.
1007 <https://doi.org/10.1175/BAMS-D-23-0230.1>
- 1008 Gelaro, R., McCarty, W., Suárez, M.J., Todling, R., Molod, A., Takacs, L., Randles,
1009 C.A., Darmenov, A., Bosilovich, M.G., Reichle, R., Wargan, K., Coy, L., Cullather,
1010 R., Draper, C., Akella, S., Buchard, V., Conaty, A., Silva, A.M. da, Gu, W., Kim, G.-
1011 K., Koster, R., Lucchesi, R., Merkova, D., Nielsen, J.E., Partyka, G., Pawson, S.,
1012 Putman, W., Rienecker, M., Schubert, S.D., Sienkiewicz, M., Zhao, B., 2017. The
1013 Modern-Era Retrospective Analysis for Research and Applications, Version 2
1014 (MERRA-2). *Journal of Climate* 30, 5419–5454. <https://doi.org/10.1175/JCLI-D-16-0758.1>
- 1015
1016 Giles, D.M., Sinyuk, A., Sorokin, M.G., Schafer, J.S., Smirnov, A., Slutsker, I., Eck, T.F.,
1017 Holben, B.N., Lewis, J.R., Campbell, J.R., Welton, E.J., Korokin, S.V., Lyapustin,
1018 A.I., 2019. Advancements in the Aerosol Robotic Network (AERONET) Version 3
1019 database – automated near-real-time quality control algorithm with improved cloud
1020 screening for Sun photometer aerosol optical depth (AOD) measurements.



- 1021 Atmospheric Measurement Techniques 12, 169–209. [https://doi.org/10.5194/amt-](https://doi.org/10.5194/amt-12-169-2019)
1022 [12-169-2019](https://doi.org/10.5194/amt-12-169-2019)
- 1023 Ginoux, P., Chin, M., Tegen, I., Prospero, J.M., Holben, B., Dubovik, O., Lin, S.-J.,
1024 2001. Sources and distributions of dust aerosols simulated with the GOCART
1025 model. *Journal of Geophysical Research: Atmospheres* 106, 20255–20273.
1026 <https://doi.org/10.1029/2000JD000053>
- 1027 Hauglustaine, D.A., Hourdin, F., Jourdain, L., Filiberti, M.-A., Walters, S., Lamarque, J.-
1028 F., Holland, E.A., 2004. Interactive chemistry in the Laboratoire de Météorologie
1029 Dynamique general circulation model: Description and background tropospheric
1030 chemistry evaluation. *Journal of Geophysical Research: Atmospheres* 109.
1031 <https://doi.org/10.1029/2003JD003957>
- 1032 Hersbach, H., Bell, B., Berrisford, P., Hirahara, S., Horányi, A., Muñoz-Sabater, J.,
1033 Nicolas, J., Peubey, C., Radu, R., Schepers, D., Simmons, A., Soci, C., Abdalla, S.,
1034 Abellan, X., Balsamo, G., Bechtold, P., Biavati, G., Bidlot, J., Bonavita, M., De
1035 Chiara, G., Dahlgren, P., Dee, D., Diamantakis, M., Dragani, R., Flemming, J.,
1036 Forbes, R., Fuentes, M., Geer, A., Haimberger, L., Healy, S., Hogan, R.J., Hólm,
1037 E., Janisková, M., Keeley, S., Laloyaux, P., Lopez, P., Lupu, C., Radnoti, G., de
1038 Rosnay, P., Rozum, I., Vamborg, F., Villaume, S., Thépaut, J.-N., 2020. The ERA5
1039 global reanalysis. *Quarterly Journal of the Royal Meteorological Society* 146, 1999–
1040 2049. <https://doi.org/10.1002/qj.3803>
- 1041 Holben, B.N., Eck, T.F., Slutsker, I., Tanré, D., Buis, J.P., Setzer, A., Vermote, E.,
1042 Reagan, J.A., Kaufman, Y.J., Nakajima, T., Lavenu, F., Jankowiak, I., Smirnov, A.,
1043 1998. AERONET—A Federated Instrument Network and Data Archive for Aerosol
1044 Characterization. *Remote Sensing of Environment* 66, 1–16.
1045 [https://doi.org/10.1016/S0034-4257\(98\)00031-5](https://doi.org/10.1016/S0034-4257(98)00031-5)
- 1046 Hu, X.-M., Klein, P.M., Xue, M., 2013. Evaluation of the updated YSU planetary
1047 boundary layer scheme within WRF for wind resource and air quality assessments.
1048 *Journal of Geophysical Research: Atmospheres* 118, 10,490-10,505.
1049 <https://doi.org/10.1002/jgrd.50823>
- 1050 Iacono, M.J., Delamere, J.S., Mlawer, E.J., Shephard, M.W., Clough, S.A., Collins,
1051 W.D., 2008. Radiative forcing by long-lived greenhouse gases: Calculations with
1052 the AER radiative transfer models. *Journal of Geophysical Research: Atmospheres*
1053 113. <https://doi.org/10.1029/2008JD009944>
- 1054 Inness, A., Ades, M., Agustí-Panareda, A., Barré, J., Benedictow, A., Blechschmidt, A.-
1055 M., Dominguez, J.J., Engelen, R., Eskes, H., Flemming, J., Huijnen, V., Jones, L.,
1056 Kipling, Z., Massart, S., Parrington, M., Peuch, V.-H., Razinger, M., Remy, S.,
1057 Schulz, M., Suttie, M., 2019. The CAMS reanalysis of atmospheric composition.
1058 *Atmos. Chem. Phys.* 19, 3515–3556. <https://doi.org/10.5194/acp-19-3515-2019>
- 1059 Jiménez, P.A., Dudhia, J., González-Rouco, J.F., Navarro, J., Montávez, J.P., García-
1060 Bustamante, E., 2012. A Revised Scheme for the WRF Surface Layer Formulation.



- 1061 Monthly Weather Review 140, 898–918. <https://doi.org/10.1175/MWR-D-11->
1062 [00056.1](https://doi.org/10.1175/MWR-D-11-00056.1)
- 1063 Jimenez, P.A., Hacker, J.P., Dudhia, J., Haupt, S.E., Ruiz-Arias, J.A., Gueymard, C.A.,
1064 Thompson, G., Eidhammer, T., Deng, A., 2016. WRF-Solar: Description and Clear-
1065 Sky Assessment of an Augmented NWP Model for Solar Power Prediction. Bulletin
1066 of the American Meteorological Society 97, 1249–1264.
1067 <https://doi.org/10.1175/BAMS-D-14-00279.1>
- 1068 Kaly, F., Marticorena, B., Chatenet, B., Rajot, J.L., Janicot, S., Niang, A., Yah, H.,
1069 Thiria, S., Maman, A., Zakou, A., Coulibaly, B.S., Coulibaly, M., Koné, I., Traoré, S.,
1070 Diallo, A., Ndiaye, T., 2015. Variability of mineral dust concentrations over West
1071 Africa monitored by the Sahelian Dust Transect. Atmos. Res. 164–165, 226–241.
1072 <https://doi.org/10.1016/j.atmosres.2015.05.011>
- 1073 Klose, M., Shao, Y., Karremann, M.K., Fink, A.H., 2010. Sahel dust zone and synoptic
1074 background. Geophysical Research Letters 37.
1075 <https://doi.org/10.1029/2010GL042816>
- 1076 Klüser, L., Killius, N., Gesell, G., 2015. APOLLO_NG – a probabilistic
1077 interpretation of the APOLLO legacy for AVHRR heritage channels. Atmospheric
1078 Measurement Techniques 8, 4155–4170. <https://doi.org/10.5194/amt-8-4155-2015>
- 1079 Kok, J.F., Adebij, A.A., Albani, S., Balkanski, Y., Checa-Garcia, R., Chin, M., Colarco,
1080 P.R., Hamilton, D.S., Huang, Y., Ito, A., Klose, M., Li, L., Mahowald, N.M., Miller,
1081 R.L., Obiso, V., Pérez García-Pando, C., Rocha-Lima, A., Wan, J.S., 2021.
1082 Contribution of the world's main dust source regions to the global cycle of desert
1083 dust. Atmos. Chem. Phys. 21, 8169–8193. [https://doi.org/10.5194/acp-21-8169-](https://doi.org/10.5194/acp-21-8169-2021)
1084 [2021](https://doi.org/10.5194/acp-21-8169-2021)
- 1085 Legates, D.R., McCabe, G.J., 2013. A refined index of model performance: a rejoinder.
1086 International Journal of Climatology 33, 1053–1056.
1087 <https://doi.org/10.1002/joc.3487>
- 1088 Marham, J.H., Parker, D.J., Grams, C.M., Grey, W.M.F., Johnson, B.T., 2008.
1089 Observations of mesoscale and boundary-layer circulations affecting dust uplift and
1090 transport in the Saharan boundary layer (preprint). [https://doi.org/10.5194/acpd-8-](https://doi.org/10.5194/acpd-8-8817-2008)
1091 [8817-2008](https://doi.org/10.5194/acpd-8-8817-2008)
- 1092 Marticorena, B., Chatenet, B., Rajot, J.L., Traoré, S., Coulibaly, M., Diallo, A., Koné, I.,
1093 Maman, A., NDiaye, T., Zakou, A., 2010. Temporal variability of mineral dust
1094 concentrations over West Africa: analyses of a pluriannual monitoring from the
1095 AMMA Sahelian Dust Transect. Atmos. Chem. Phys. 10, 8899–8915.
1096 <https://doi.org/10.5194/acp-10-8899-2010>
- 1097 Marticorena, B., Dorego, G.S., Rajot, J.L., Bouet, C., Allègre, M., Chatenet, B., Féron,
1098 A., Gaimoz, C., Siour, G., Valorso, R., Diop, M., Der Ba, S., Rokhy N'Diaye, G.,
1099 Séné, M. & Thiam, A. (2021). Air temperature, Bambey, Senegal. [dataset]. Aeris.
1100 <https://doi.org/10.25326/263>



- 1101 Marticorena, B., Dorego, G.S., Rajot, J.L., Bouet, C., Allègre, M., Chatenet, B., Féron,
1102 A., Gaimoz, C., Maisonneuve, F., Siour, G., Valorso, R., Diop, M., Der Ba, S.,
1103 Rokhy N'Diaye, G., Séné, M. & Thiam, A. (2021). PM10 concentration, Bambey,
1104 Senegal. [dataset]. AERIS. <https://doi.org/10.25326/267>
- 1105 Mazzeo, A., Burrow, M., Quinn, A., Marais, E.A., Singh, A., Ng'ang'a, D., Gatari, M.J.,
1106 Pope, F.D., 2022. Evaluation of the WRF and CHIMERE models for the simulation
1107 of PM_{2.5} in large East African urban conurbations. Atmospheric Chemistry and
1108 Physics 22, 10677–10701. <https://doi.org/10.5194/acp-22-10677-2022>
- 1109 Menut, L., 2023. Variability and combination as an ensemble of mineral dust forecasts
1110 during the 2021 CADDIWA experiment using the WRF 3.7.1 and CHIMERE
1111 v2020r3 models. Geoscientific Model Development 16, 4265–4281.
1112 <https://doi.org/10.5194/gmd-16-4265-2023>
- 1113 Menut, L., Bessagnet, B., Briant, R., Cholakian, A., Couvidat, F., Mailler, S., Pennel, R.,
1114 Siour, G., Tuccella, P., Turquety, S., Valari, M., 2021. The CHIMERE v2020r1
1115 online chemistry-transport model. Geoscientific Model Development 14, 6781–
1116 6811. <https://doi.org/10.5194/gmd-14-6781-2021>
- 1117 Menut, L., Siour, G., Mailler, S., Couvidat, F., Bessagnet, B., 2016. Observations and
1118 regional modeling of aerosol optical properties, speciation and size distribution over
1119 Northern Africa and western Europe. Atmos. Chem. Phys. 16, 12961–12982.
1120 <https://doi.org/10.5194/acp-16-12961-2016>
- 1121 MODIS Atmosphere Science Team, 2017. MODIS/Terra Aerosol Cloud Water Vapor
1122 Ozone Daily L3 Global 1Deg CMG. https://doi.org/10.5067/MODIS/MOD08_D3.061
- 1123 Niu, G.-Y., Yang, Z.-L., Mitchell, K.E., Chen, F., Ek, M.B., Barlage, M., Kumar, A.,
1124 Manning, K., Niyogi, D., Rosero, E., Tewari, M., Xia, Y., 2011. The community
1125 Noah land surface model with multiparameterization options (Noah-MP): 1. Model
1126 description and evaluation with local-scale measurements. Journal of Geophysical
1127 Research: Atmospheres 116. <https://doi.org/10.1029/2010JD015139>
- 1128 Ochiegbu, D.C., 2021. Event of harmattan dust transport in Kano State of Nigeria.
1129 IJSRP 11, 205–210. <https://doi.org/10.29322/IJSRP.11.08.2021.p11628>
- 1130 Plain, N., Hingray, B., Mathy, S., 2019. Accounting for low solar resource days to size
1131 100% solar microgrids power systems in Africa. Renewable Energy 131, 448–458.
1132 <https://doi.org/10.1016/j.renene.2018.07.036>
- 1133 Prigent, C., Jiménez, C., Catherinot, J., 2012. Comparison of satellite microwave
1134 backscattering (ASCAT) and visible/near-infrared reflectances (PARASOL) for the
1135 estimation of aeolian aerodynamic roughness length in arid and semi-arid regions.
1136 Atmospheric Measurement Techniques 5, 2703–2712. <https://doi.org/10.5194/amt-5-2703-2012>
- 1137
1138 Prospero, J.M., Ginoux, P., Torres, O., Nicholson, S.E., Gill, T.E., 2002. Environmental
1139 Characterization of Global Sources of Atmospheric Soil Dust Identified with the
1140 Nimbus 7 Total Ozone Mapping Spectrometer (toms) Absorbing Aerosol Product.
1141 Reviews of Geophysics 40, 2-1-2–31. <https://doi.org/10.1029/2000RG000095>



- 1142 Qu, Z., Oumbe, A., Blanc, P., Espinar, B., Gesell, G., Gschwind, B., Klüser, L., Lefèvre,
1143 M., Saboret, L., Schroedter-Homscheidt, M., Wald, L., 2017. Fast radiative transfer
1144 parameterisation for assessing the surface solar irradiance: The Heliosat-4 method.
1145 Meteorologische Zeitschrift 33–57. <https://doi.org/10.1127/metz/2016/0781>
- 1146 Rajot, J.L., Abdourhamane Touré, A., Marticorena, B., Bouet, C., Allègre, M., Chatenet,
1147 B., Féron, A., Gaimoz, C., Siour, G., Valorso, R., Maman, A. & Zakou, A. (2010). Air
1148 temperature, Banizoumbou, Niger. [dataset]. AERIS. <https://doi.org/10.25326/210>
- 1149 Rajot, J.L., Boubacar, A., Marticorena, B., Bouet, C., Allègre, M., Chatenet, B., Féron,
1150 A., Gaimoz, C., Siour, G., Valorso, R., Coulibaly, S.B., Kouyaté, Z., Coulibaly, B.,
1151 Coulibaly, M., Koné, I. & Traoré, S. (2010). Air temperature, Cinzana, Mali.
1152 [dataset]. AERIS. <https://doi.org/10.25326/269>
- 1153 Rajot, J.L., Boubacar, A., Marticorena, B., Bouet, C., Allègre, M., Chatenet, B., Féron,
1154 A., Gaimoz, C., Maisonneuve, F., Siour, G., Valorso, R., Coulibaly, S.B., Kouyaté,
1155 Z., Coulibaly, B., Coulibaly, M., Koné, I. & Traoré, S. (2010). PM10 concentration,
1156 Cinzana, Mali. [dataset]. AERIS. <https://doi.org/10.25326/268>
- 1157 Redelsperger, J.-L., Diedhiou, A., Flamant, C., Janicot, S., Lafore, J.-P., Lebel, T.,
1158 Polcher, J., Bourlès, B., Caniaux, G., Rosnay, P. de, Desbois, M., Eymard, L.,
1159 Fontaine, B., Geneau, I., Ginoux, K., Hoepffner, M., Kane, C.S.E., Law, K.S., Mari,
1160 C., Marticorena, B., Mougin, É., Pelon, J., Peugeot, C., Protat, A., Roux, F., Sultan,
1161 B., Akker, E. van den, 2006. Amma, une étude multidisciplinaire de la mousson
1162 ouest-africaine. La Météorologie 54, 22. <https://doi.org/10.4267/2042/20098>
- 1163 Sawadogo, W., Fersch, B., Bliefernicht, J., Meilinger, S., Rummeler, T., Salack, S., Guug,
1164 S., Kunstmann, H., 2024. Evaluation of the WRF-solar model for 72-hour ahead
1165 forecasts of global horizontal irradiance in West Africa: A case study for Ghana.
1166 Solar Energy 271, 112413. <https://doi.org/10.1016/j.solener.2024.112413>
- 1167 Schepanski, K., Tegen, I., Todd, M.C., Heinold, B., Bönisch, G., Laurent, B., Macke, A.,
1168 2009. Meteorological processes forcing Saharan dust emission inferred from MSG-
1169 SEVIRI observations of subdaily dust source activation and numerical models.
1170 Journal of Geophysical Research: Atmospheres 114.
1171 <https://doi.org/10.1029/2008JD010325>
- 1172 Schroedter-Homscheidt, M., Azam, F., Betcke, J., Hanrieder, N., Lefevre, M., Saboret,
1173 L., Saint-Drenan, Y.-M., 2022. Surface solar irradiation retrieval from MSG/SEVIRI
1174 based on APOLLO Next Generation and HELIOSAT-4 methods. Meteorologische
1175 Zeitschrift 31, 455–476.
- 1176 Shao, Y., Lu, H., 2000. A simple expression for wind erosion threshold friction velocity.
1177 Journal of Geophysical Research: Atmospheres 105, 22437–22443.
1178 <https://doi.org/10.1029/2000JD900304>
- 1179 Skamarock, W.C., Klemp, J.B., Dudhia, J., Gill, D.O., Barker, D.M., Duda, M.G., Huang,
1180 X.-Y., Wang, W., Powers, J.G., n.d. A Description of the Advanced Research WRF
1181 Version 3.



- 1182 The Paris Agreement | UNFCCC [WWW Document], n.d. URL
1183 <https://unfccc.int/process-and-meetings/the-paris-agreement> (accessed 2.12.24).
- 1184 Thompson, G., Eidhammer, T., 2014. A Study of Aerosol Impacts on Clouds and
1185 Precipitation Development in a Large Winter Cyclone. *Journal of the Atmospheric*
1186 *Sciences* 71, 3636–3658. <https://doi.org/10.1175/JAS-D-13-0305.1>
- 1187 Tuccella, P., Menut, L., Briant, R., Deroubaix, A., Khvorostyanov, D., Mailler, S., Siour,
1188 G., Turquety, S., 2019. Implementation of Aerosol-Cloud Interaction within WRF-
1189 CHIMERE Online Coupled Model: Evaluation and Investigation of the Indirect
1190 Radiative Effect from Anthropogenic Emission Reduction on the Benelux Union.
1191 *Atmosphere* 10, 20. <https://doi.org/10.3390/atmos10010020>
- 1192 Vautard, R., Bessagnet, B., Chin, M., Menut, L., 2005. On the contribution of natural
1193 Aeolian sources to particulate matter concentrations in Europe: Testing hypotheses
1194 with a modelling approach. *Atmospheric Environment* 39, 3291–3303.
1195 <https://doi.org/10.1016/j.atmosenv.2005.01.051>
- 1196 Washington, R., Todd, M.C., 2005. Atmospheric controls on mineral dust emission from
1197 the Bodélé Depression, Chad: The role of the low level jet. *Geophysical Research*
1198 *Letters* 32. <https://doi.org/10.1029/2005GL023597>
- 1199 Washington, R., Todd, M.C., Lizcano, G., Tegen, I., Flamant, C., Koren, I., Ginoux, P.,
1200 Engelstaedter, S., Bristow, C.S., Zender, C.S., Goudie, A.S., Warren, A., Prospero,
1201 J.M., 2006. Links between topography, wind, deflation, lakes and dust: The case of
1202 the Bodélé Depression, Chad. *Geophysical Research Letters* 33.
1203 <https://doi.org/10.1029/2006GL025827>
- 1204 Wild, O., Zhu, X., Prather, M.J., n.d. Fast-J: Accurate Simulation of In- and Below-Cloud
1205 Photolysis in Tropospheric Chemical Models.
- 1206 Willis, P.T., Tattelman, P., 1989. Drop-Size Distributions Associated with Intense
1207 Rainfall. *Journal of Applied Meteorology* (1988-2005) 28, 3–15.
- 1208 Yang, D., Bright, J.M., 2020. Worldwide validation of 8 satellite-derived and reanalysis
1209 solar radiation products: A preliminary evaluation and overall metrics for hourly data
1210 over 27 years. *Solar Energy, Special Issue on Grid Integration* 210, 3–19.
1211 <https://doi.org/10.1016/j.solener.2020.04.016>
- 1212 Yushchenko, A., De Bono, A., Chatenoux, B., Kumar Patel, M., Ray, N., 2018. GIS-
1213 based assessment of photovoltaic (PV) and concentrated solar power (CSP)
1214 generation potential in West Africa. *Renewable and Sustainable Energy Reviews*
1215 81, 2088–2103. <https://doi.org/10.1016/j.rser.2017.06.021>
- 1216 Zhang, L., Gong, S., Padro, J., Barrie, L., 2001. A size-segregated particle dry
1217 deposition scheme for an atmospheric aerosol module. *Atmospheric Environment*
1218 35, 549–560. [https://doi.org/10.1016/S1352-2310\(00\)00326-5](https://doi.org/10.1016/S1352-2310(00)00326-5)
- 1219 Ziane, A., Necaibia, A., Sahouane, N., Dabou, R., Mostefaoui, M., Bouraiou, A., Khelifi,
1220 S., Rouabhia, A., Blal, M., 2021. Photovoltaic output power performance
1221 assessment and forecasting: Impact of meteorological variables. *Solar Energy* 220,
1222 745–757. <https://doi.org/10.1016/j.solener.2021.04.004>